Investigation of radiofrequency reflectometry in group-IV spin-qubit devices

Johanna Malina Zeis
Supervisor: Prof. Ferdinand Kuemmeth
Co-Supervisor: Prof. Saskia Fischer
A thesis presented for the degree of
M.Sc. in Physics

KØBENHAVNS UNIVERSITET

Faculty of Science
Copenhagen University
Danmark
04.05.2024

Acknowledgements

I would like to thank everyone who helped me during this masters project. I would like to thank Ferdinard Kuemmeth for taking on the role of my supervisor and allowing me to participate in the spin qubit group. I would also like to thank Saskia Fischer for assuming the role of my co-supervisor and giving me valuable advice. Thank you Harry Lampadaris and Anton Zubchenko for assisting me in navigating a laboratory that was entirely new to me. I would also like to thank Harry for his invaluable assistance throughout this entire master's project, providing me with a comprehensive understanding of the diverse facets of the experiments. I am indebted to William Lawrie for his guidance in the field of silicon germanium, and to Vasilis Vlachodimitropoulos for his insights into gallium arsenide. Thank you Tsung-Lin Chung for teaching me about QCodes and the digital aspects of the laboratory. My participation in the spin qubit group has been a highly valuable experience and I also want to thank the remaining spin qubit group members for that. Lastly, I would like to thank my parents and my partner Leon because you were and are always there for me.

Contents

1 Introduction

In this thesis I introduce the concept lateral, gate-defined single and double quantum dots (DQDs). I'll introduce experimatal methods of charge sensing, noise mesurements and most importantly the topic of radiofrequency reflectometry.

Radiofrequency reflectometry plays a pivotal role in the pursuit of implementing qubits within semiconductor quantum dots, offering invaluable insights into their behavior and enabling precise characterization. As qubits in semiconductor quantum dots are highly sensitive to environmental fluctuations, accurate measurement techniques are essential for their manipulation and control. Radiofrequency reflectometry provides a non-invasive means to probe the charge occupancy and electron spin states of quantum dots, allowing to monitor their dynamics and optimize conditions for qubit operation.

The first experiment discussed in this thesis is conducted on a GaAs component to test the transmission lines of the Kiutra cryostat. The objective is to find out if it is possible to conduct RF reflectometry experiments in this cryostat. Following this, the second experiment will involve investigating a SiMOS component, initially focusing on charge sensing and tuning of quantum dots through DC measurements. Subsequently, the aim will be to replicate these findings using RF reflectometry measurements. The third device, a Ge/SiGe device, will undergo experiments from two distinct categories. Firstly, a sensor dot and a double quantum dot will be tuned using RF reflectometry. Secondly, noise measurements will be performed on two samples of the Ge/SiGe component, with power spectral density being calculated and reference values at 1Hz extracted and compared with literature values. The objective of this experiment is to compare a device fabricated by members of the spin qubit qroup in local cleanrooms to state of the art devices.

2 Theoretical foundations of gate controlled quantum dot spin-qubit structures

2.1 Quantum information

An analogy between bits and qubits

Todays most common computers process information classically using bits as their fundamental units of information. How information can also be processed through quantum systems is described in quantum information theory. In this theory, qubits, analog to classical bits, form the fundamental units of information. The Bloch-sphere (Fig.1) can graphically illustrate the difference between classical bits and qubits. It is a unit sphere, often defined with a north and south pole, similarly to the earth. The classical bit can be described by a single variable with two distinct values, defined to be 0 and 1. In the Bloch-sphere, these states are recovered from two vectors, one to each pole. In contrast, the qubit's state is represented by an arbitrary vector, $|\Psi\rangle$, that can be directed to any point on the surface of the Bloch sphere. This implies a qubit can be in the same state as a classical bit, in fact, $|0\rangle$ and $|1\rangle$ are the basis states. However, the qubit can also be in an infinite number of other states determined by a phase ψ. Physically, these additional states are explained by the fact that a qubit can exist in superposition of two states we earlier defined as $|0\rangle$ and $|1\rangle$.

$$|\Psi\rangle = \alpha|0\rangle + \beta|1\rangle \tag{1}$$

The complex probability amplitudes α and β are associated with the probabilities $P_0 = |\alpha|^2$ and $P_1 = |\beta|^2$, respectively for finding the qubit in either state $|0\rangle$ or $|1\rangle$. The following normalization condition holds: $|\alpha|^2 + |\beta|^2 = 1$.

$$|\Phi\rangle = cos\Big(\frac{\Theta}{2}\Big)|0\rangle + e^{i\psi}sin\Big(\frac{\Theta}{2}\Big)|1\rangle \tag{2}$$

with $\Theta \in [0, \pi]$ and $\psi \in [0, \frac{\pi}{2}]$.

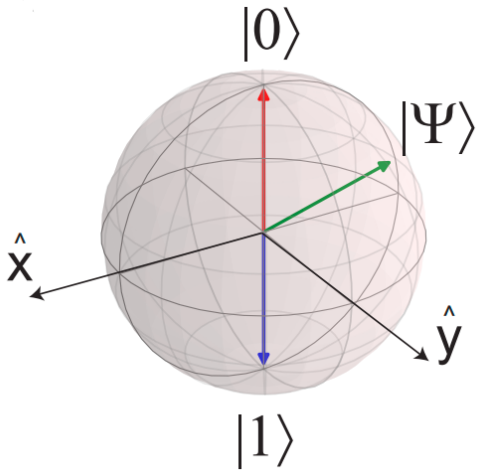

Figure 1: The Bloch-sphere as a graphical representation of qubits. The vectors $|0\rangle$ (red) and $|1\rangle$ (blue) are the basis vectors, the vector $|\Psi\rangle$ (green) represents a general qubit state[1].

To gain more insight into the implications of the quantum nature of qubits, consider an arbitrary two-qubit state. First look at:

$$|\Psi\rangle_a = \alpha_a|0\rangle + \beta_a|1\rangle \tag{3}$$

and

$$|\Psi\rangle_b = \alpha_b|0\rangle + \beta_b|1\rangle \tag{4}$$

, which are two single qubit states. They are located in separable Hilbert spaces and connected through a tensor product $|\Psi\rangle_{a,b} = |\Psi\rangle_a \otimes |\Psi\rangle_b$. The two qubit state then is given by:

$$|\Psi\rangle_{a,b} = \alpha_a\alpha_b|00\rangle + \alpha_a\beta_b|01\rangle + \beta_a\alpha_b|10\rangle + \beta_a\beta_b|11\rangle \tag{5}$$

A quantum computer's computational power doubles with each additional qubit ($\propto 2^M$ with M being the number of qubits), while a 'classical' computer's computational power increases linearly with the number of its bits ($\propto 2N$ with N being the number of bits).

DiVincenzo criteria

DiVincenzo's criteria idenitify a set of five prerequisites for the implementation of a quantum computing system in an experimental setting, taken from sources [12] and [13].

1) A scalable physical system with well characterized qubits

2) The ability to initialize the qubit's state Before starting computations, the register should be initialised to a known state.

3) Long relevant decoherence times Coherence is defined as the property in which the phase relationship between different components of the state remains constant over time. Decoherence disrupts the coherent superposition of quantum states, causing them to rapidly lose their phase information and thus their quantum properties, resulting in classical behaviour.

4) A universal set of quantum gates A universal set of gates is a set of quantum logic gates that, when combined, can be used to approximate any quantum operation with arbitrary precision.

5) The capability to measure the qubit's state (fast) To extract information from qubits, their state has to be measured.

2.2 The connection between coherence and noise

Noise can impair the coherence properties of quantum states, leading to decoherence and the loss of quantum information. Various types of noise, including charge noise and environmental noise, can affect the coherence of quantum dot devices. One approach to reducing noise levels, is to minimise thermal fluctuations and suppress electronic noise sources. This can be achieved by applying cryogenic temperatures to quantum dot devices. This reduction in noise contributes to enhanced coherence in the quantum dot system. All measurements in this thesis are carried out in cryostats at temperatures in the millikelvin regime. Another approach that can help to reduce noise, is a very clean and precise production of the components and their underlying heterostructures. Longer integration times can also improve signal quality by reducing noise. However, longer integration times increase the likelihood of encountering decoherence, which can lead to a deterioration

in the signal-to-noise ratio rather than an improvement. This highlights the delicate balance required in experimental designs to optimise measurement quality while minimising the impact of decoherence on the system. Ideally, the readout would be fast and have low impact on the qubit's state.

2.3 Readout and why it needs to be fast

In order to minimise the impact of noise and decoherence processes, it is essential to employ fast readout in quantum dot devices. This enables efficient quantum state measurement and control. Faster readout rates allow for higher bandwidth measurements and improved dynamic range. The bandwidth refers to the range of frequencies over which a system can effectively operate or measure signals. A wider bandwidth allows for the probing of a wider range of frequencies. At higher frequencies, noise, such as 1/f noise, is less pronounced, thus rapid readout rates assist in the acquisition of quantum information before it is lost to decoherence mechanisms. How can we achieve the ideal regime of large bandwidths where measurements are both rapid and have low noise? This can be achieved with the help of radiofrequency reflectometry, which will be discussed in chapter 3.2.

2.4 Gate controlled quantum dot structures

Single quantum dot

Quantum dots are nanometer-scale physical systems. They confine charge carriers, that can be either holes or electrons, in all three dimensions. The system's scale is comparable to that of the fermi wavelength, resulting in quantised energy levels, similar to those in real atoms. Quantum dots offer a promising platform for implementing qubits due to their ability to confine single or few charge carriers in a well-defined quantum state, enabling precise control and manipulation. In this thesis, confinement is achieved by combining bandgap engineering of heterostructures with electrostatic gating. Before going into a more detailed explanation of this confinement structure, it should be mentioned that gate controlled quantum dot structures ideally operate in either accumulation or depletion mode. If all gates are set to 0 V and there is a current, the device is operating in depletion mode. If there is no current, it is in accumulation mode. For the sake of simplicity, the following theoretical chapters only consider gate structures designed for devices

operating in accumulation mode.

Figure 2a depicts a schematic of a single quantum dot implemented through an arbitrary semiconductor heterostructure. The charge carriers (two exemplary white dots) are vertically confined by the heterostructure (grey). They accumulate under the plunger gate (blue) and are shielded from the reservoirs (green) by surrounding barrier gates (red). In Figure 2a charge carriers are blocked from the reservoir, the dot is in blockade regime. On the other hand, there is directional transport of charge carriers through the dot in Figure 2b, which means it is in transport regime. It is possible for the two aforementioned regimes to be alternated, this being initiated by a change in the voltage applied to the plunger gate. Figure 2e depicts sharp current peaks at certain gate voltages, indicating transport through the dot. In between them there is no current, transport is blocked. A thorough examination of the potential that confines the carriers laterally provides the desired explanation. Figures 2c and 2d display the quantised energy levels via chemical potentials μ_N, enclosed between two reservoirs with different voltages applied to them. The voltage difference leads to a difference in chemical potential and, along with the lever arm α, this defines the source-drain-bias $V_{SD} = \alpha(\mu_S - \mu_D)$. If one or more energy levels lie within the bias window (dashed lines), charge carriers can be transported through the quantum dot due to the quantum tunnel effect (compare again Fig 2b and 2d). In the case of no energy levels within the bias window, the charge carriers do not have enough energy to tunnel through the barrier. The classical Coulomb repulsion makes it energetically unfavourable for more than N charge carriers to occupy the dot, hence N is named the dot's charge occupancy.

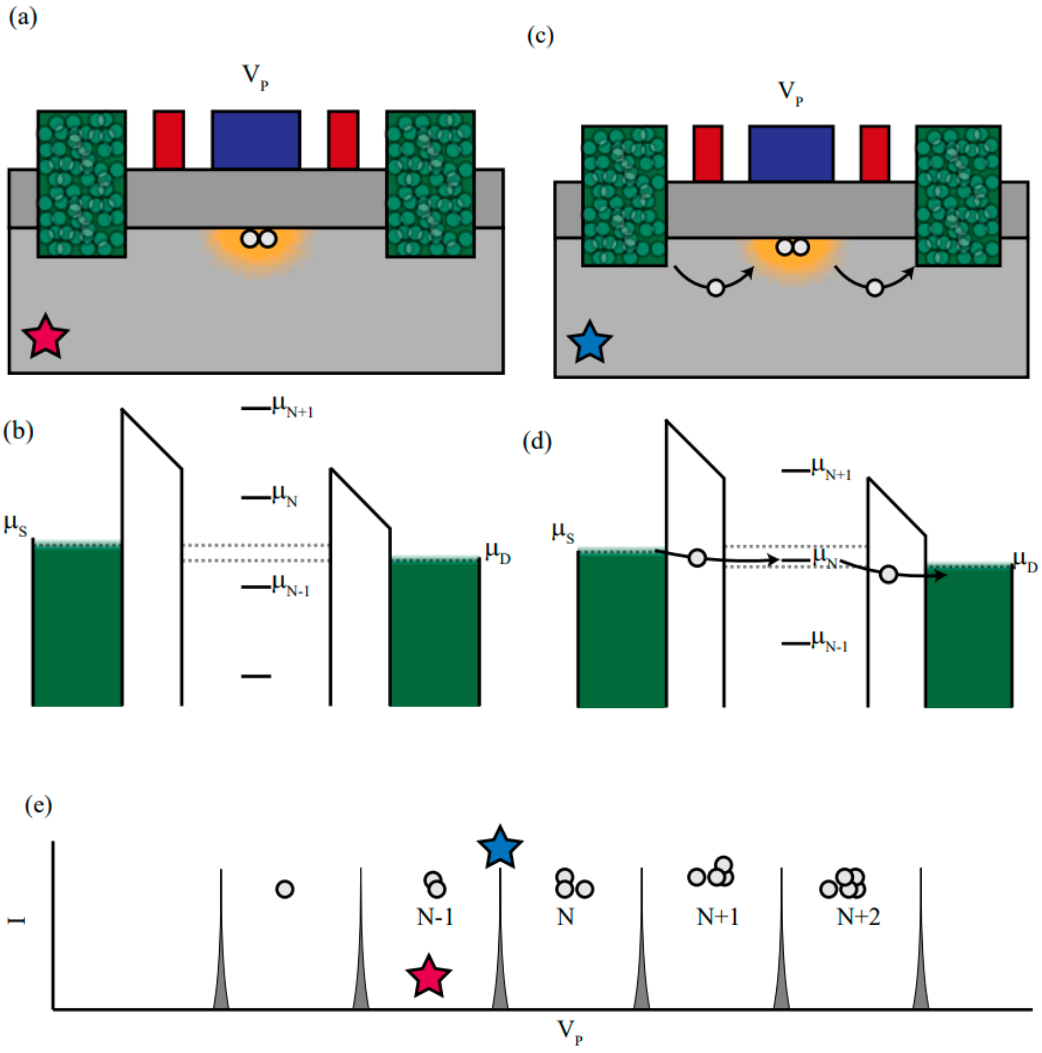

Figure 2: Schematic illustration of transport through gate controlled quantum dot structures. Taken from [1].

By sweeping the source/drain bias over the plunger gate, we can observe Coulomb diamonds (Fig. 3), which provide valuable information about the quantum dot. Inside the Coulomb diamonds, the number of electrons is fixed and no current flows (white area). Outside the Coulomb diamonds, the number of electrons fluctuates and current flows (blue or red area). As the bias increases, there may also be several states that lie within the bias window and for which transport is therefore energetically favourable. These regions

are indicated by darker colours in the schematic diagram. The charging energy, which is the energy required to add another electron to the quantum dot, is equal to half the height of the Coulomb diamonds. Thus, assuming there is no offset in the Coulomb diamonds, it is determined by measuring from $V_{SD} = 0$ to the top peak as indicated in figure 3 by the dashed line. The lever arm can also be determined by the relationship between the total width and half the height of the Coulomb diamond:

$$\alpha = \frac{|\Delta V_{SD}|}{|\Delta V_G|} \tag{6}$$

were ΔV_{SD} is half the height and ΔV_G is the width [20].

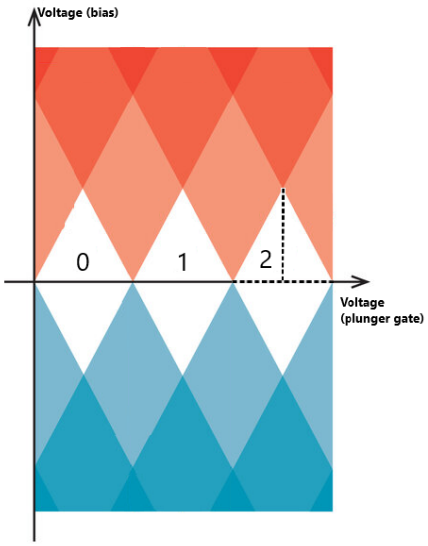

Figure 3: A schematic stability diagram showing Coulomb diamonds. Areas with blocked current are white, areas with one energetically allowed charge state transition are bright (blue or red), and areas with two energetically allowed charge state transitions are darker (blue or red). The vertical dashed line indicates the half of the height of one of the Coulomb diamonds which is equal to the charging energy. The horizontal dashed line indicates the width of the Coulomb diamond. Adapted from source 17.

Double quantum dot

Only a single quantum dot is needed to implement a Loss-DiVincenzo qubit, which is the simplest and one of the first spin qubits. However, other more advanced spin qubits, such as the singlet-triplet qubit, can only be implemented using two (or more) coupled quantum dots [3]. The next logical step is therefore to introduce the concept of the double quantum dot (DQD). The confinement structure is similar to that of an SQD (Fig. 4). Now there are two plunger gates (blue) that cause charge carriers to accumulate in the underlying heterostructure. The barrier gate (red) between these two plungers can control the interdot-coupling which comprises tunnel coupling and capacitive coupling.

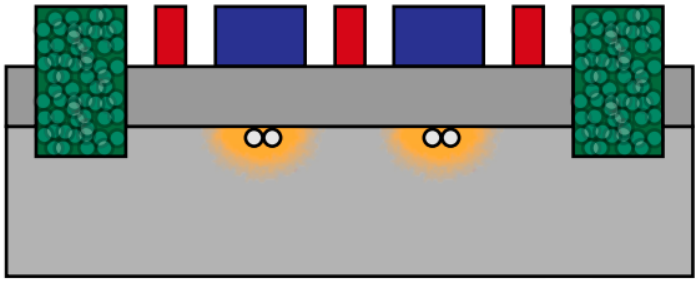

Figure 4: Schematic representation of a general DQD structure. Adapted from [1].

In a stability diagram, the conductance through a DQD is measured as a function of both plunger gate voltages. The conductance resonances exhibit varying patterns changing with the interdot coupling, as can be seen in figure 5. Each cell in this pattern corresponds to an equilibrium number of charge carriers the DQD has for the respective configuration of gates. In the first stability diagram in figure 5 the two quantum dots (QDs) are completely decoupled. Looking at the rectangular pattern of the charge transitions it becomes evident, that the number of charges in dot 1 can only be changed by plunger gate V_{g1} and vice versa V_{g2} only affects the charges in dot 2. There are now two adjacent single quantum dots (SQDs). The second diagram in figure 5 displays a stability diagram with increased interdot-coupling. There is a honneycomb-pattern where the vertices of the square domains have separated. This separation is caused by tunnel-coupling. Due to capacitive coupling, each plunger gate now influences the charges in both dots. Further

increase in the coupling results in the stability diagrams depicted in third diagram of figure 5. The diagram shows a single, large dot, with charge N1+N2 and equal coupling to both plunger gates, as indicated by the slope of the transitions.

Worth noting:

1) The diagram depicts the system's behaviour in linear transport regime, where there is a minimal bias voltage ($V_{SD} \approx 0\,V$) between the source and drain. When a finite source-drain bias is applied, shifting into the non-linear transport regime, the triple points transform into triangular shapes.

2) The cross-capacitive coupling between gates and QDs, as well as between plunger gates, is omitted in this discussion. In practice, cross-capacitances change the gradient of the charge domain boundaries.

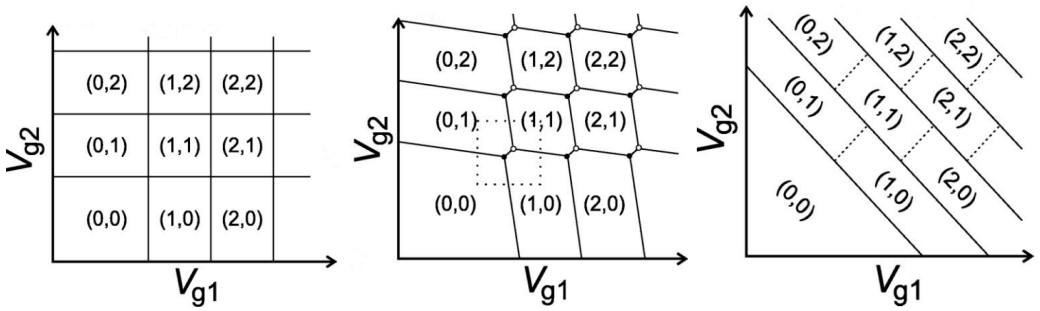

Figure 5: Schematic representation of the stability diagram in three different coupling regimes [6].

3 Experimental methods

3.1 Charge sensing

Charge sensing is used to obtain the charge stability diagram of quantum dot structures by monitoring the changes in the conductance of an adjacent sensor dot. A top view of a gate structure suitable for measuring a single quantum dot is shown in Figure 6a. The sensor dot is capacitively coupled to the SQD. It is essential that there is no tunneling between the dots, as this would not only affect the readout signal, but also the state of the SQD, possibly resulting in decoherence. The sensor dot is calibrated to detect sharp Coulomb peaks. The plunger gate voltage is then set to the point with the largest slope of the Coulomb peak, as this is where the conductance is most sensitive to changes in the electric field. A change in the number of charge carriers in the neighbouring quantum dot is accompanied by a change in the electric field at the SQD. As there is a capacitive coupling between the SQD and the sensor dot, the electric field of the sensor dot also changes. Figure 6b illustrates the Coulomb peak of the sensor dot, with the red star indicating the initial position and the differently coloured stars visuallyising the change in the SQD with the addition of charge carriers. The changes visualised by the stars can then be displayed in an IV-diagram as shown in Figure 6c. Every time the plunger gate voltage is changed by more than αE_{add}, there is a change in the charge occupation of the dot.

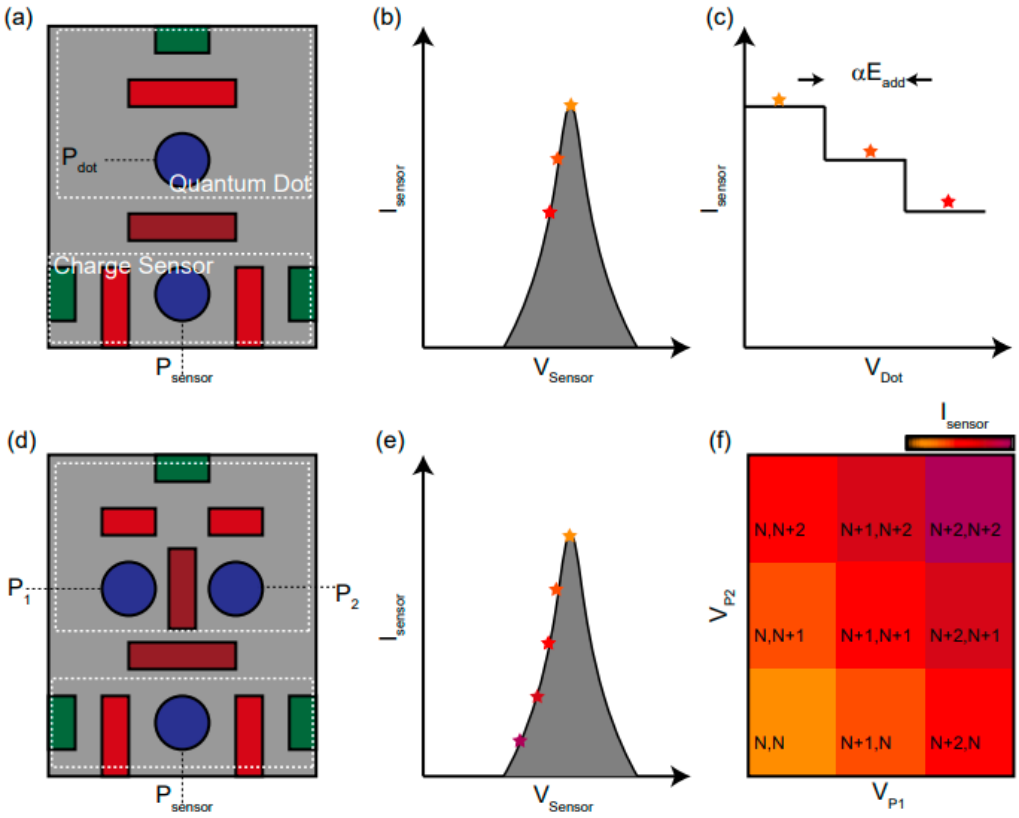

Figure 6: Schematic illustration of the physical theory behind the charge sensing method. Adapted from [1].

Charge sensing for DQDs is largely analogue to the process for SQDs. As can be seen in Figure 6f, the differently coloured rectangles reproduce the stability diagram presented in section 2.4. The colour scale is defined by the capacitance, which is measured at the sensor dot and varies with the position on the Coulomb peak. N+1 charge carriers are initially assumed in both dots and then varied.
Worth noting:

QD charge sensors can reach higher sensitivity than single electron transistors (sharper conductance peaks) and quantum point contacts (steeper slope). However, the QD's charge sensors sensitivity drops away after one Coulomb peak, reducing its dynamic range to charge sensing signals.

3.2 Radiofrequency reflectometry

As previously outlined in Chapter 2.2 and 2.3, a broad bandwidth and high frequencies are important for keeping noise low and to be able to implement fast readout. In measurements employing direct transport, the bandwidth is limited by several factors including the resistance R of the sample and the capacitance C of the transmission lines. This can also be interpreted as a RC low-pass filter, where R is usually on the order of a few tens of $k\Omega$ and $C = 0.1\,nF - 1\,nF$ [7]. The formula for the cutoff frequency of a low-pass filter is given by $f_{cut} = \frac{1}{2\pi RC}$, which results in the cutoff frequency beeing limited to a few kHz. Unfortunately, the level of noise present at low frequencies is particularly noticeable. For instance, the 1/f noise can be significant below 10 kHz. Radiofrequency reflectometry can yield an immense increase in the operational frequency and bandwidth, which not only allows operating the device above the 1/f noise, but also enables higher speed in the measurements [7]. Instead of measuring the transport of charge carriers, the idea is to measure the change in a radio frequency sent to, and reflected from the device. The RF signal travels along a transmission line towards the device. The device functions as a resistive component, whose value is contingent upon its settings. The RF signal is then reflected on the device, with the voltage reflection coefficient beeing $\Gamma(\omega)$. Through homodyne detection the reflected signal is compared to the original signal, with the change in amplitude monitored in order to ascertain the charge state of the quantum dots. $\Gamma(\omega)$ depends upon the relationship between the characteristic impedance Z_0 and the impedance of the load $Z_l(\omega)$, that in turn depends on the angular frequency ω of the RF signal. As of now, Z_0 is equal to the impedance of the transmission line (around $50\,\Omega$) and $Z_l(\omega)$ is equal to the impedance of the device:

$$\Gamma(\omega) = \frac{Z_l(\omega) - Z_0}{Z_l(\omega) + Z_0} \tag{7}$$

When a RF signal encounters an impedance mismatch between the characteristic impedance and the load impedance, which means either $Z_l(\omega) >> Z_0$ or $Z_l(\omega) << Z_0$, $\Gamma(\omega)$ becomes large. This implies that the majority of the RF signal is reflected back to its source. In the case of quantum devices, it is almost always $Z_l(\omega) >> Z_0$, which also indicates that the change

in the amplitude of the reflected RF signal is barely dependent on $Z_l(\omega)$. This problem can be resolved by incorporating an additional inductor L and capacitor C into the circuit to match $Z_l(\omega)$ to Z_0 (Fig. 7). This is called a matching network. The impedance matching process maximises the transfer of power from the source to the load, while simultaneously minimising the reflection coefficient.

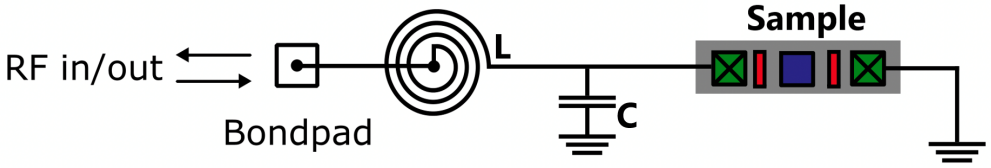

Figure 7: Schematic diagram of the impedance matching circuit, comprising inductor (L), capacitor (C), and the sample in the cryostat. All components of the circuit are connected in series and there is a ground behind the capacitor and the sample. The RF signal is fed into the circuit via the bondpad and then sent to the gate structures via the ohmic contact marked in green, where it is then reflected back depending on the gate settings of the sample.

For the sake of deeper understanding, it makes sence to introduce parasitic resistors, as can be seen in figure 8. They model dissipation in the circuit. RL represents ohmic losses in the inductor, while RC models dielectric losses in the capacitor. The impedance of this circuit, acting as a load on the transmission line, is defined by equation

$$Z_l = j\omega L_C + R_L + \frac{R_{eq}}{1 + j\omega R_{eq} C_P} \tag{8}$$

,where R_{eq} is $R_{eq} = R_S || R_C$ (parallel combination). On resonance the imaginary part of equation 8 is $Im(Z_l) = 0$, which leads to the following expression for the resonance frequency

$$f_{LCR} = \frac{1}{\sqrt{LC}} \tag{9}$$

,where $\frac{L_C}{R_{eq}^2 C_P} << 1$ has to hold. This means that the resonance frequency of the matching network can be approximated by an LCR circuit as long as the conditions mentioned above are met.

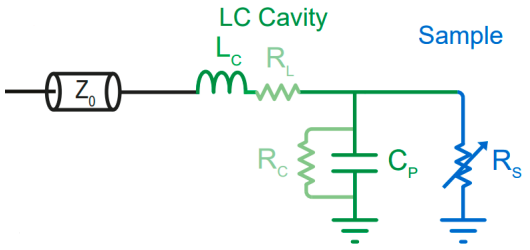

Figure 8: Schematic diagram of the impedance matching circuit, comprising the characteristic impedance Z_0, the inductor (L_C) with resistance R_L, the capacitor (C_P) with resistance R_C, and the sample (R_S). Adapted from [7].

From equation 9 it becomes apparent, that the frequency at which resonance occurs in the circuit does not depend on the resistance of the circuit. This configuration is optimal for measuring the change in RF amplitude, as the peak does not maintain its position at a constant L and C as intended, but only its amplitude. This was already evident from equation 7, which remains valid in this context. A visualisation of the measured RF signal is provided in Figure 9a, which is contrasted with an RF signal in which L and C were also changed (Fig. 9b).

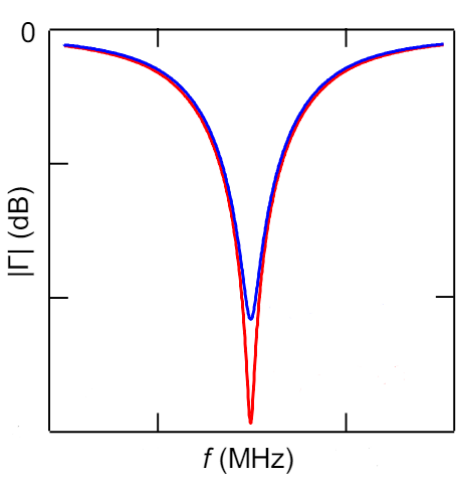

(a) Schematic representation of the variation of the amplitude in the rf signal. Adapted from Source 8

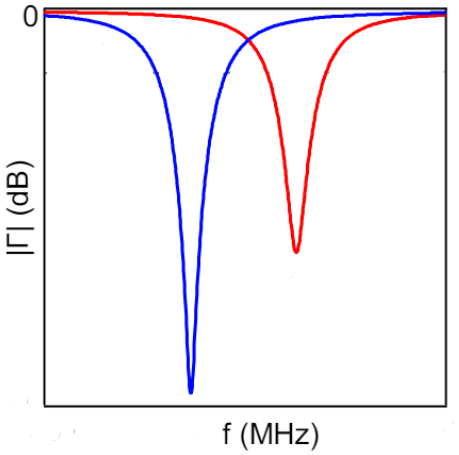

(b) Schematic representation of the variation of the amplitude and the resonance frequency in the rf signal. Adapted from Source 8

Figure 9

Composition of the signal

In the context of RF reflectometry, the terms I (in-phase), Q (quadrature), R (amplitude), and phase (Ψ) are essential parameters used to characterise the reflected RF signal. The in-phase component I represents the magnitude of the signal that is in phase with the reference signal. It provides information about the magnitude or strength of the reflected signal. The quadrature component Q represents the magnitude of the signal that is 90 degrees out of phase with the reference signal. It provides information about the phase difference between the reflected signal and the reference signal. The amplitude, often denoted as R, represents the overall strength or magnitude of the reflected RF signal. It is a combination of both the in-phase (I) and quadrature (Q) components. In RF reflectometry, R is calculated as the square root of the sum of squares of the I and Q components ($R = \sqrt{I^2 + Q^2}$). The phase represents the angular displacement of the reflected signal with respect to the reference signal. This indicates the phase shift between the two signals [21]. Depending on the setup used to perform RF reflectometry, different combinations of the above variables are measured, from which the signal is then reconstructed. An overview of the centrepieces of the RF setups im-

plemented in the scope of this project and the quantities measured can be found in Table 1.

Centrepiece of the setup	Detected physical quantities
Demod.Circuit	I
UHF-Li	I,Q,R,Ψ
VNA	R,Ψ
OPX	I,Q,R,Ψ

Table 1: An overview of the centrepieces of the RF setups implemented in the scope of this project and the quantities measured.

3.3 Noise measurements

The number of points (Npts = 2000) and the sampling interval (Sampling = 0.08s) had to be choosen before starting the measurements. The following two paragraphs describe their influence.

The number of points in a measurement determines the total duration of the measurement and, as a consequence, sets the lowest frequency that can be resolved. This is because the frequency resolution in a Fourier transform is determined by the total duration of the signal being transformed. A longer duration (more data points) allows for the resolution of lower frequencies. Consequently, the Npts parameter denotes the lowest frequency that can be resolved in an FFT analysis.

The sampling interval specifies the frequency with which data points are recorded or sampled during the measurement. A shorter sampling interval allows for the capture of data points at a higher frequency, which enables the capture of higher frequencies in the signal. Conversely, a longer sampling interval limits the highest frequency that can be accurately captured. This is due to the Nyquist-Shannon sampling theorem, which states that in order to accurately reconstruct a signal, the sampling frequency must be at least twice the highest frequency present in the signal. Consequently, a shorter sampling interval is associated with a higher sampling frequency, which enables the capture of higher frequencies in the signal.

Current

The noise measurements commence with the measurement of the current over a specified time interval. Initially, the voltage bias must be selected. In the context of this thesis, the case in which a quantum dot has already been tuned, so that the Coulomb diamonds and Coulomb peak are present, is relevant. Accordingly, the voltage bias can be selected so that the voltage is approximately halfway up the Coulomb diamond. Subsequently, a series of noise measurements can be conducted in which the plunger gate voltage is set at different points on the Coulomb peak. The various current-noise measurements can then be plotted in a single plot. It should become clear that a larger current is measured with a higher position on the Coulomb peak. Depending on the stability of the state in the device, one or more jumps may occur, which are charging events. Charging events occur when additional charges are added to, or removed, from the quantum dot, typically due to changes in the electrostatic environment.

PSD

The drain current noise spectrum S_I is also assessed at different peak sensitivities located on the flanks and the peak of a choosen Coulomb peak, as well as next to it in Coulomb blockade regime. The different current noise spectra are then transformed into charge noise spectra using the formula

$$PSD = \alpha\sqrt{S_I}\Big(\frac{dI}{dV}\Big)^{-1} \tag{10}$$

,where α represents the lever arm of the quantum dot, and $\frac{dI}{dV}$ is the slope of the Coulomb peak [19]. The power spectral density (PSD) can then be plotted over the frequency that can be obtained through a fast Fourier transform of the time-axis of the current noise.

1/f noise

The 1/f noise, also known as flicker noise, is a type of noise whose PSD is inversely proportional to the frequency f of the signal. To look for 1/f noise in a fit, the PSD is typically plotted as a function of frequency, where the noise amplitude scales inversely with frequency. A common approach is to utilise a power-law model, such as $PSD(f) = \frac{A}{f^\gamma}$, where A represents the noise amplitude and γ denotes the scaling exponent. Should the fitting

of noise with a simple power-law model prove inadequate in capturing the experimental data, additional terms may be introduced to the model. These may take the form of $PSD(f) = \frac{A}{f^{\alpha}} + \frac{B}{f^{\beta}}$, where $\frac{B}{f^{\beta}}$ provides an additional component in the model, thereby allowing for the accounting of deviations from the simple power-law behaviour [18].

4 Experimental setups and devices

As part of my research project, I conducted measurements on three devices in different experimental setups. The central component of the first setup is a Kiutra cryostat, which is based on the principle of adiabatic demagnetization refridgeration (ADR). In the second setup, it is a dilution refrigerator (DR) from Bluefors. A list of key data for both cryostats can be found in the appendix. Table 2 provides an overview of the experimental setups used in this work, as well as the components measured in each case.

Device material	Cryostat	Measurements
GaAs	Kiutra (ADR)	DC, RF using UHF-Li
SiMOS	Kiutra (ADR)	DC, RF using Demod.C., UHF-Li, VNA
Ge/SiGe	Bluefors (DR)	DC, RF using OPX

Table 2: Description of measurements for different devices sorted by the materials they are based on.

4.1 DC setup - fridge independent

The signal entering the dilution refrigerator is generated by a digital-to-analog converter. In the scope of this project the converter is a QDAC2 by Quantum Machines. Each electrical connection of the quantum device is linked to one of the output channels of the QDAC2 for individual adressability of each gate and ohmic contact. The QDAC2 is connected to a breakout box through BNC coaxial cables. The breakout box permits individual connection ("float") and grounding ("ground") of its channels through miniature switches. After the breakout box the signal enters the dilution refridgerator that cools the sample down to temperatures in the millikelvin regime. Subsequently, the current returning from the sample goes through a current preamplifier (Ithaco), before beeing measured with a digital multimeter (Agilent Keysight). The measurements are performed with ohmic contacts beeing under a voltage bias. There are also measurements that can be performed on this setup with a current bias, but this is not part of this project. This setup is depicted in figure 10.

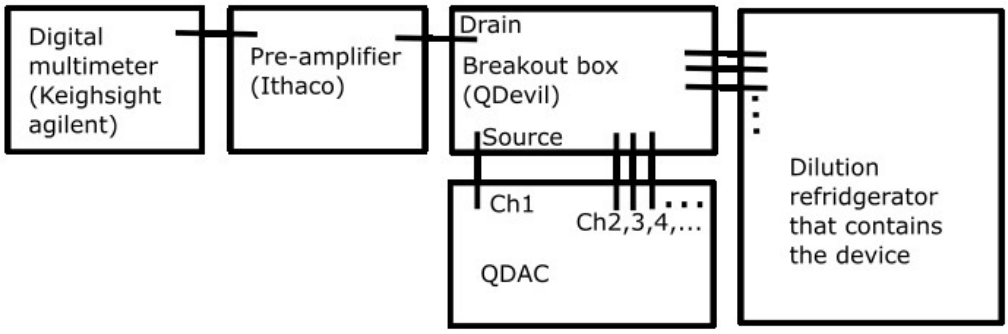

Figure 10: Schematic representation of a cryostat-independent experimental setup for DC measurements.

Figure 11 presents a similar setup for DC transport, in which an additional lock-in amplifier is implemented and the Ithaco has been replaced with a Basel.
Lock-in amplifiers are designed to extract and measure the amplitude and phase of a signal at a specific frequency of interest. This is particularly useful in scenarios where the signal is noisy. The lock-in amplifier generates a reference signal that is applied to the sample. This reference signal typically has a well-defined amplitude and phase. The reference signal is mixed (multiplied) with the signal coming back from the cryostat through a process called homodyne detection. The resulting mixed signal is then passed through a low-pass filter, letting only the frequency of interest pass. It is important to emphasise the difference to measurements without lock-in. Without a lock-in the voltage or the current is measured, whereas the lock-in measures the differential voltage and the differential current.

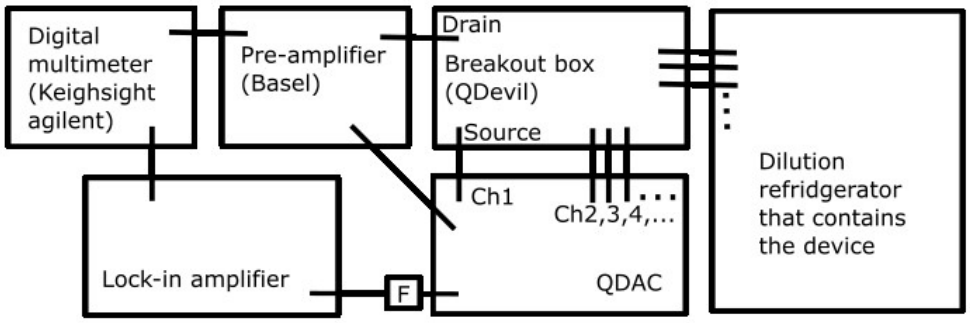

Figure 11: Schematic representation of a cryostat-independent experimental setup for DC measurements.

4.2 Three different reflectometry setups in Kiutra

Demodulation circuit

A carrier signal is generated and delivered to the sample in the cryostat. The demodulation mechanism depends on the multiplication of the carrier signal with the reflected and amplified signal from the reflection line (Rx). The result is manifested as an electrical waveform with a detectable DC component, the magnitude of which is directly correlated to the amplitude of the reflected carrier signal. This is the basic principle behind RF reflectometry using a demodulation circuit. To implement this experiment, closer attention needs to be payed to the circuit, its components and how they work, because the different components need to be tuned to each other.
A sine wave signal is generated by a signal generator operating at the resonant frequency of the sample board. This signal is passed through a directional coupler with the primary output going to the RF mixer and the coupled output going to the sample. The RF mixer has three connections: L, R and I, corresponding to the local oscillator (L), RF input and intermediate frequency (I) ports respectively. The RF mixer performs signal multiplication, which is part of the homodyne detection in the demodulation circuit. Synchronisation between local oscillator (L) and radio frequency (RF) signals is important, with in-phase signals providing peak output amplitudes and out-of-phase signals reducing it. To overcome this, a phase shifter is integrated into the sample-facing output circuit, allowing voltage-dependent phase modulation and hence demodulated output adjustment. This phase

shifter allows the phase of the signal to be changed within a range of 0 to 180 degrees depending on the applied voltage. To reduce noise, high and low pass filters are implemented because they cut off unwanted frequencies that are either too high or too low. When administering electrical signals to the device, care must be taken to avoid applying excessive power, which could lead to unwanted perturbations in the quantum state of the device or even damage it. Therefore, a programmable attenuator was used before the signal entered the cryostat, allowing manual adjustment of the attenuation levels. Precise attenuation settings were fine-tuned to optimise the signal-to-noise ratio for a single charge sensor, resulting in a sample power application of 70 dB.

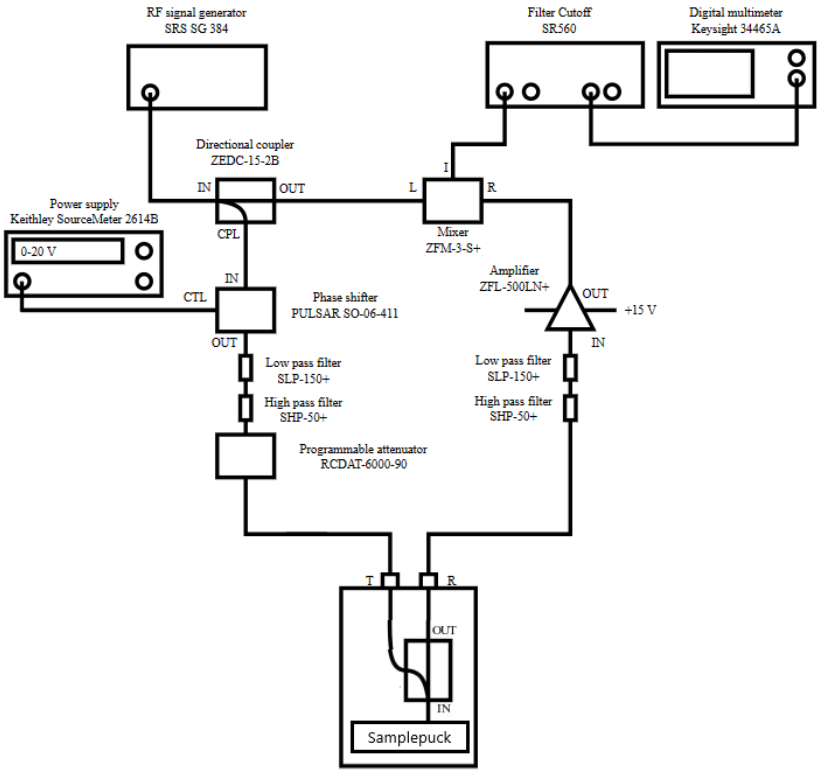

Figure 12: Schematic representation of a experimental setup for RF measurements using a demodulation circuit. Taken and adapted with kind permission from Charalampos Lampadaris.

The signal enters the cryostat via the T-port, where it is subjected to

attenuation by further attenuators. The specifics of the interior of Kiutra are not included in this section. However, a comprehensive overview of Kiutra's interior can be found in the appendix. Finally, the signal is routed to the sample through a decoupler. The signal reflected there is separated from the incoming signal via the decoupler and exits the cryostat via the R port after passing through an amplifier. At room temperature, the signal passes through a second amplifier to amplify it further before readout. In the mixer, the signal is then mixed with the reference signal and converted from AC to a DC signal, which is then read out by the digital multimeter.

UHF-Li

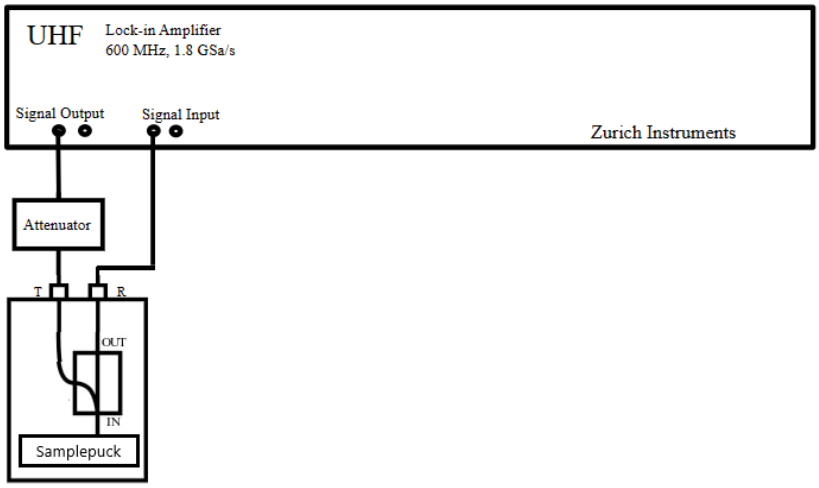

Figure 13: Schematic representation of a experimental setup for RF measurements using an UHF-Li.

The Zurich Instruments UHF-Li is a digital lock-in amplifier that is widely used for high-frequency operation. It is capable of operating at a wide frequency range, spanning from DC to 600 MHz. With a rapid time constant of 30 ns for demodulation, it ensures precise signal processing, facilitating demodulation bandwidths exceeding 5 MHz. Its integration with the LabOne instrument control software streamlines user interaction and enhances overall usability. The UHF-Li replaces the entire demodulation circuit. In order to prevent the excitation signal from reaching the QD at a level that would result in the heating of the charge carriers or even damage to the device, it

is necessary to ensure that the amplitude of the signal is kept low (approx. 70 dB). For this reason, and in order to achieve a higher signal-to-noise ratio at the output, an attenuator is to be added at the output of the UHF-Li. Otherwise, the connection to the T port and the R port and thus to the cryostat is the same as for the demodulation circuit.

Vector network analyzer

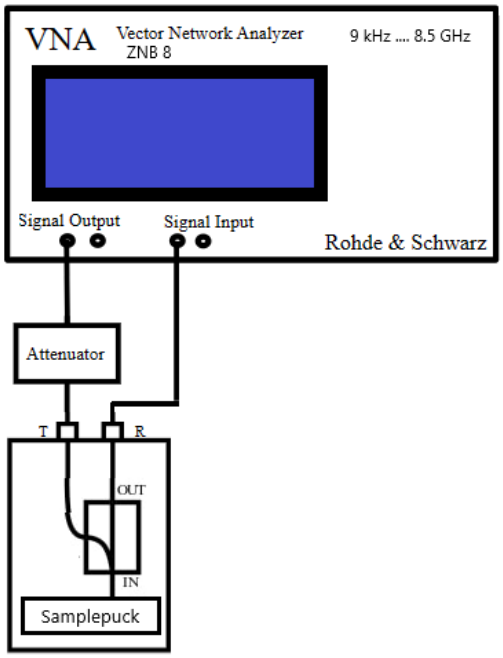

Figure 14: Schematic representation of a experimental setup for RF measurements using a VNA.

The Vector Network Analyzer (VNA) has a wide frequency range spanning from 9 kHz to 8.5 GHz, rendering it suitable for a multitude of radio frequency (RF) applications. Its range of intermediate frequency (IF) bandwidths extends from 1 Hz to 10 MHz. With the capacity to generate a known stimulus signal and simultaneously measure the induced changes in a device, the VNA is equipped with up to four integrated sources. The closed-loop configuration facilitates highly accurate measurements of the electrical magnitude R and phase response of components. The device is equipped with a Windows-based

control software and a dedicated screen for displaying the measured signal. Analogous to the UHF-Li, the addition of an attenuator at the output of the VNA is necessary to achieve a higher signal-to-noise ratio at the output. Additionally, the connection to the T port and the R port, and thus to the cryostat, is identical to that of the demodulation circuit and the UHF-Li.

4.3 Reflectometry setup in Bluefors

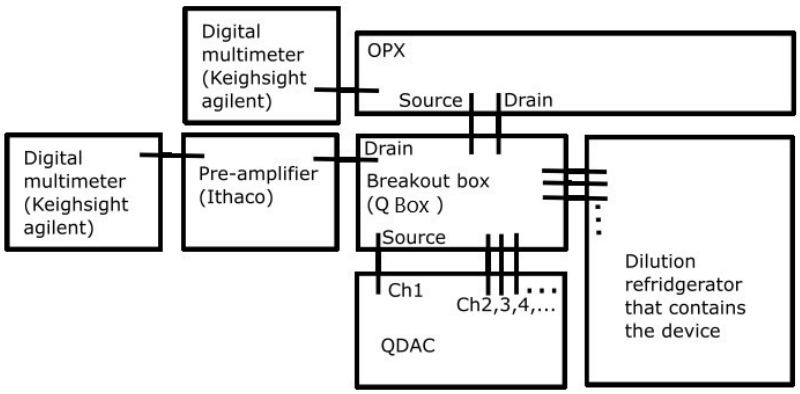

Figure 15: Schematic representation of a experimental setup for RF measurements using an OPX.

In an RF setup utilising an OPX, several instruments are interconnected as illustrated in Figure 15. A digital multimeter (DMM) is linked to a pre-amplifier, which enhances the sensitivity of incoming signals. The pre-amplifier is then connected to a breakout box, which serves as a central hub for signal routing. Concurrently, a quantum dot array controller (QDAC2) is connected to the same breakout box, enabling precise manipulation of quantum dot devices. Additionally, a second DMM is directly linked to the OPX, a pulse generator and measurement system. This enables time-domain reflectometry (TDR) measurements and pulse generation. Furthermore, the OPX is connected to the breakout box, establishing communication with other instruments in the setup. Finally, the breakout box is connected to the cryostat through fast lines (RF lines) and slow lines (DC lines), sending a signal to the sample.

4.4 GaAs device

The device was developed by Federico Fedele as part of his PhD-project at Copenhagen University. GaAs/AlGaAs is a common material pairing for creating a two-dimensional electron gas (2DEG), since the materials have identical lattice constants and crystal structures to allow strain-free growth on top of each other [16]. However, when a thin layer of AlGaAs is deposited on top of GaAs, discrepancies in lattice constants, and consequently band gaps, arise between the two materials. This dissonance induces strain at their interface, culminating in the formation of a quantum well [9]. The 2DEG consists of a layer of electrons that can move in two dimensions, while being confined in the third dimension by the heterostructure (Fig. 16). It forms at the junction between the two different semiconductors with different band gaps. The semiconducting material is coated with an oxide and metal gates. By applying different voltages to the metal gate, the resulting electric field can manipulate the electrons in the gas below, forming a potential well. This allows the electrons to be localised in a one-dimensional channel below the gate, thereby controlling the device conduction through the metal gate. This confinement can lead to the creation of quantum dots or double dots.

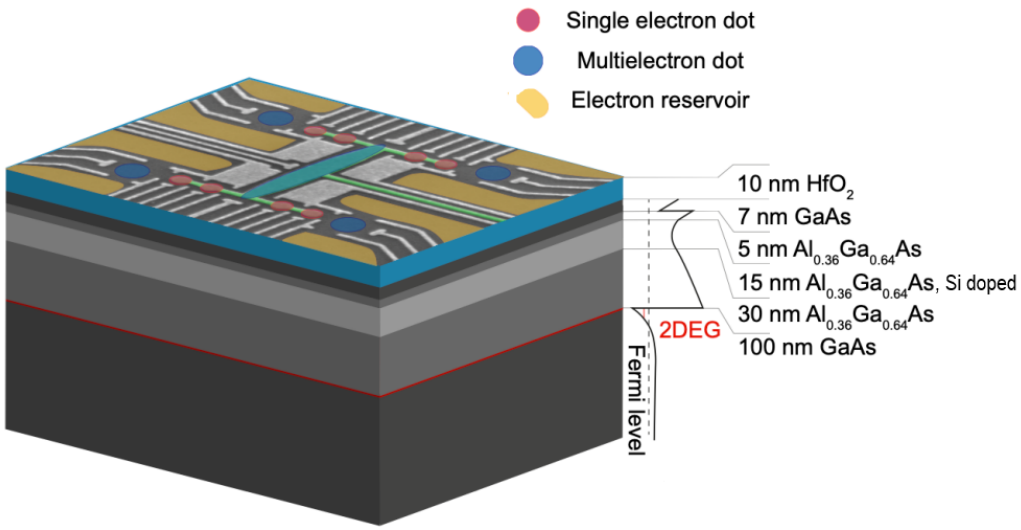

Figure 16: Schematic cross-sectional view of the GaAs component with a detailed representation of the potential of the heterostructure. Adapted from [11].

The split gate structure of the device consists of four quadrants. Each quadrant contains two ohmic contacts that can be biased or connected to an RF signal generator. Four surface-mount inductors with different inductances are connected to an ohmic contact (Fig. 17). The technique of multiplexing allows the device to have multiple tank circuits with different resonant frequencies. The metal gate structure contains plunger and barrier gates. The yellow gate in the centre is used to couple the qubits within the device.

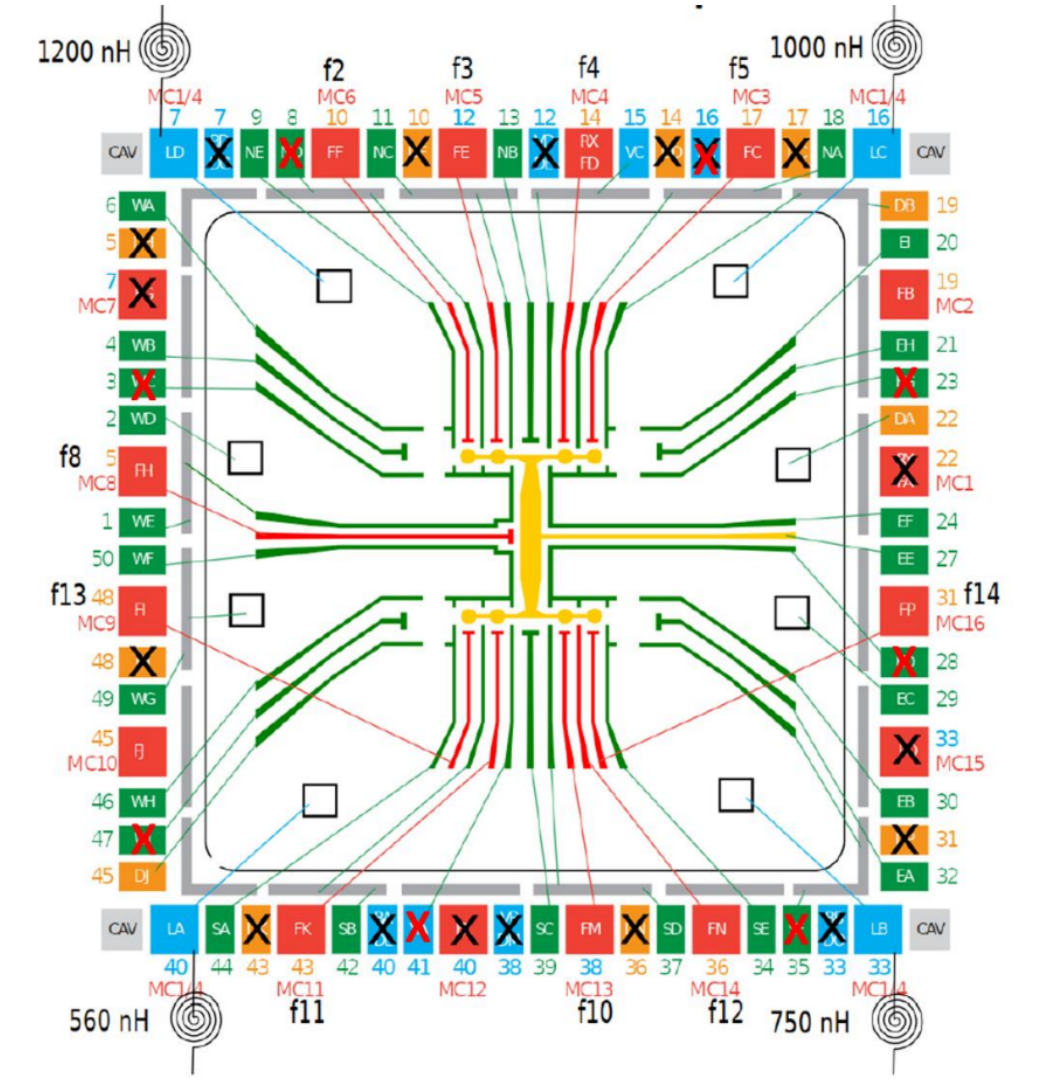

Figure 17: The pinout diagram of the GaAs component [9].

The component in question exhibits functional limitations, which are attributable to both broken bonds and the test setup. In the pinout diagram (Fig. 17), the inoperability of the gates is indicated by black and red crosses. In addition, the ohmic quadrant in the upper quadrant is not functional for measurements in DC transport.

4.5 SiMOS device

This device was manufactured by Imec, a leading research and innovation hub in nanoelectronics and digital technologies. Figure 18a illustrates a double dot with a charge sensor and its circuit equivalent [15]. The silicon metal-oxide-semiconductor (SiMOS) structure in quantum dot devices typically comprises several layers with distinct physical properties. The silicon substrate serves as the foundation of the device. It provides a crystalline structure for the subsequent layers and serves as a platform for the formation of quantum dots. The SiO_2 layer serves as an insulating oxide barrier between the semiconductor layers and the metal gates. It helps to electrically isolate the gates from the semiconductor, preventing unwanted leakage currents. Then there are the metal gate structures (in red, blue and green) at three different height levels.

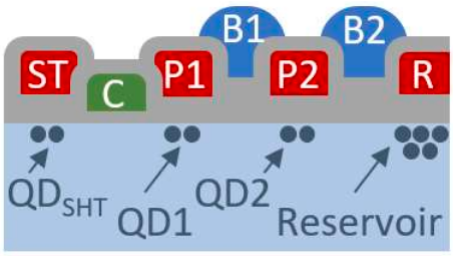

(a) Schematic cross-section [15].

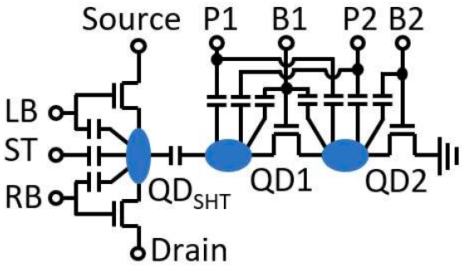

(b) The circuit equivalent [15].

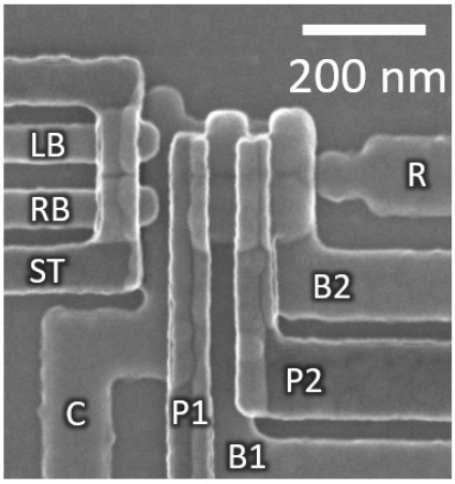

(c) Top down SEM image [15].

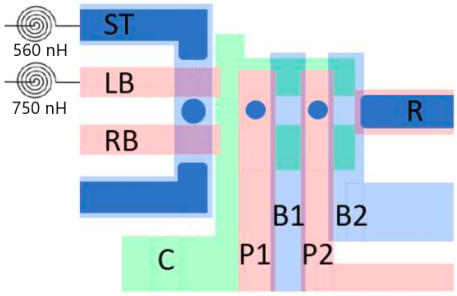

(d) Top down schematic image [15].

Figure 18

The scanning electron microscopy (SEM) image (Fig.18c) displays qubit gates designed for double quantum dots and a charge sensor dot. The various gates are distributed across a total of three levels. The first of these is the C gate, which restricts the two-dimensional electron gas in one dimension. Then there is the R gate that provides charge carriers. The charge carriers accumulate under the plunger gates (P1 and P2), which are shielded from the reservoir by the barrier gate B2. The barrier gate B1 determines the coupling or the degree of shielding between the two quantum dots. The sensor dot is located in close proximity to the C-gate and in the vicinity of the two quantum dots. The ST gate is employed here to capture charge carriers from the 2DEG in one dimension. The left and right barriers (LB and RB) trap the charge carriers in a further dimension, which then defines the sensor point. Figure 18d displays the same gate structure as presented on the SEM

image. Figure 18b presents the circuit equivalent, which primarily illustrates the various couplings. The plunger and barrier gates are capacitively coupled to the quantum dots. Additionally, the quantum dots and the sensor point are also capacitively coupled to each other. Furthermore, there is a tunnel coupling between the two quantum dots and to the reservoir R, via which charge carriers enter both quantum dots. The ST gate also acts as a source and drain for the sensor quantum dot, and therefore there is also a tunnel coupling here. There are two surface mount inductors, one is connected to the ST gate with an inductance of $560\,nH$ and the other one is connected to the LB barrier gate with an inductance of $750\,nH$.

4.6 Ge/SiGe device

This component was fabricated by Charalampos Lampadaris in the clean rooms of University of Copenhagen as part of his PhD-project. The process of crystal growth is conducted on Si wafers (Fig. 19). A virtual substrate (VS) is defined as a structure comprising a Si buffer layer, followed by the addition of a relaxed Ge layer. This VS is then used as the basis for the growth of the reverse linear graded (RLG) buffer layer, which begins with a 100% concentration of Ge and progresses to a Si_XGe_{1-X} alloy with a composition of $Si_{0.2}Ge_{0.8}$. This growth process contributes to the formation of a compressively strained Ge layer, which hosts a two-dimensional hole gas (2DHG). Consequently, the charge carriers in this component are holes.

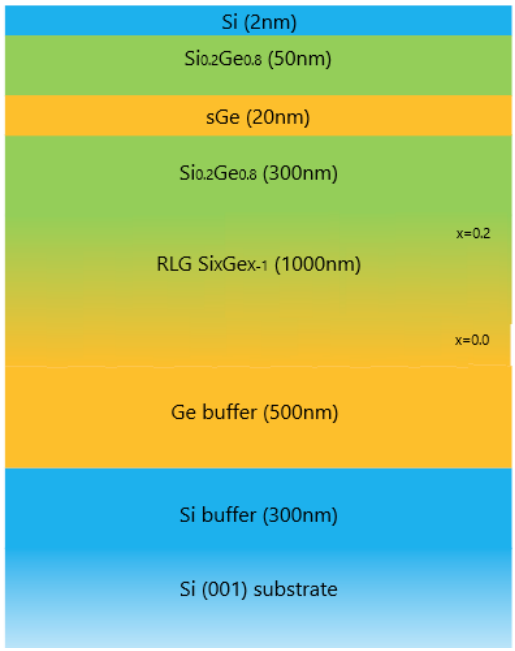

Figure 19: Schematic cross-sectional view of the Ge/SiGe device. Taken with kind permission from Charalampos Lampadaris.

The gate structure forms a quadruple quantum dot structure with quantum dots arranged in a row (Fig. 20a,b). Additionally, there are two sensor quantum dots, one of which is located at each end of the row of quantum dots. There are two surface mount inductors, both connected to ohmic contacts with one having an inductance of $1200\,nH$ and the other one having an inductance of $750\,nH$.

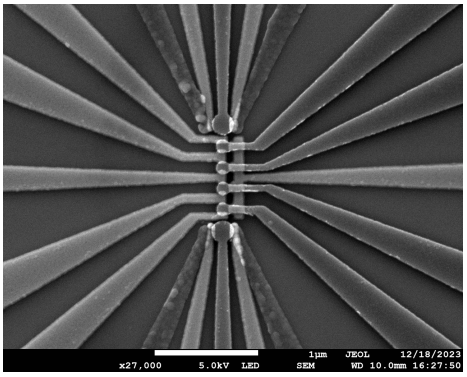

(a) Top down SEM image. Taken with kind permission from Charalampos Lampadaris.

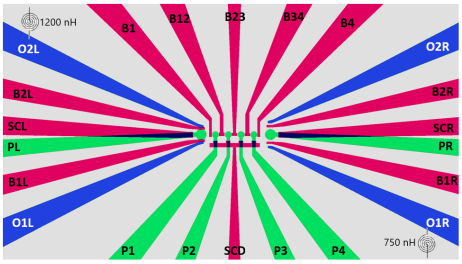

(b) Top down schematic image. Taken with kind permission from Charalampos Lampadaris.

Figure 20

5 Measurement results and discussion

5.1 Testing of rf lines in Kiutra using a GaAs device

Regarding the notation in the following paragraph: The gates and the ohmic contacts are labelled according to the bond pads, which can be seen in the pinout diagram for the component in chapter 4.4.

The aim is to test whether a radio frequency signal can be sent to the device through RF-lines in Kiutra and whether changing the gate settings will also result in a change in the signal. For this purpose, the GaAs device was used, as radio frequency measurements have already been successfully performed on this device [9].

First, the resonant frequencies of the four tank circuits are detected. Therefore, the power of the RF signal is set to -40 dBm and the UHF-Li is used for all of the measurements (Chapter 4.2). Prior to any of the resonance dips belonging to tank circuits, the background spectrum is measured by keeping all gates open (0 V). In the background signal, there is a pronounced dip in reflection amplitude at approximately 100 MHz. A comparable background spectrum exhibiting a dip at the same frequency was subsequently documented by other members of the spin-qubit research group, who conducted analogous experiments on other devices with a comparable experimental setup. The next steps were to pinch off the gates. Two to three gates were simultaneously set from 0 V to -1 V. Now it is important to note that the signal arrives at the component via multiplexing. This implies that the reflectometry signal is always received by all four circuits. By pinching off with different gates, the resistive part of the respective gate changes. It can for example be seen in figure 17, that for the upper left quadrant the gates 6 and 9 are pinched of. Subsequently, all four resonance dips occurred for the frequency that matched the resonance of the circuit around which the gates were located. The background dip coincides with the resonance dip observed in the circuit located in the lower right quadrant, with a inductance of 750 nH. Due to this overlap, the dip is less pronounced compared to the other three. Table 3 gives an overview over the circuits and the pinched-off gates, as well as the measured resonant frequencies.

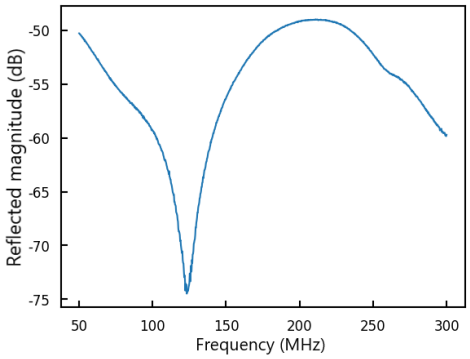

Figure 21: The background signal

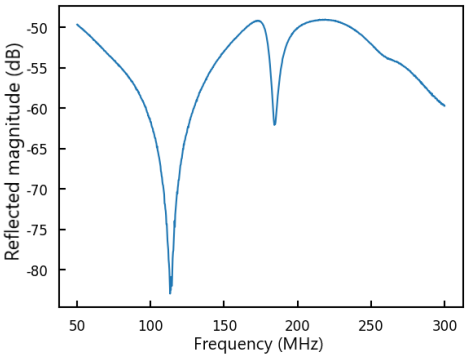

Figure 22: Resonance dip of bottom left LC circuit

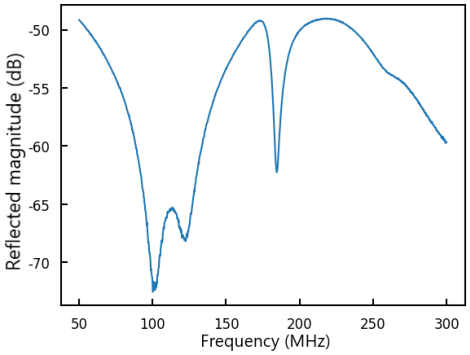

Figure 23: Resonance dip of the bottom right LC circuit

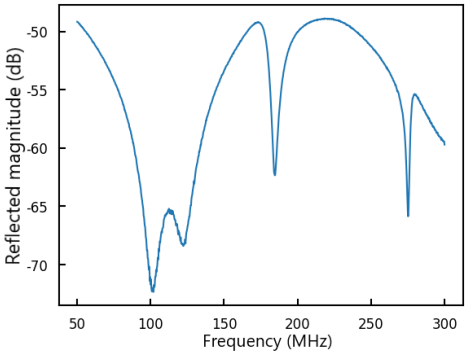

Figure 24: Resonance dip of the top right LC circuit

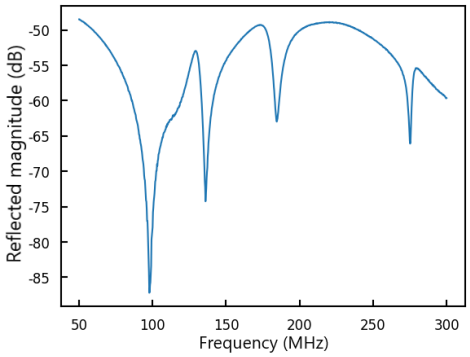

Figure 25: Resonance dip of the top left LC circuit

Circuit sorted by inductance L	Pinched-off gates (named after bond pads)	Rf resonance frequency
$1200\,nH$	06, 09	$137.5\,MHz$
$1000\,nH$	19, 20	$274.8\,MHz$
$750\,nH$	30, 32, 34	$101\,MHz$
$560\,nH$	44, 45	$186\,MHz$

Table 3: Overview over the circuits and the pinched-off gates, as well as the resonance frequencies.

According to equation 9, the resonance frequencies are proportional to the inductivity L of the inductor and the capacitance C of the conductor. In an ideal scenario, the capacitance would be identical for all four circuits, resulting in an increase in resonance frequencies as the inductance values decrease. Upon examination of Table 3, it becomes evident that the resonant frequencies do not adhere to the mentioned ideal scenario. It is important to note that the ohmic contact in the upper right quadrant is permanently earthed and thus the electronic environment is shaped differently than it is supposed to, which could potentially result in a shift in the resonant frequency. Other reasons for the two shifted resonance frequencies could be parasitic capacitance from nearby components or interconnects, that might affect the effective capacitance in each quadrant differently as well as heterogeneity in gate materials or fabrication processes.

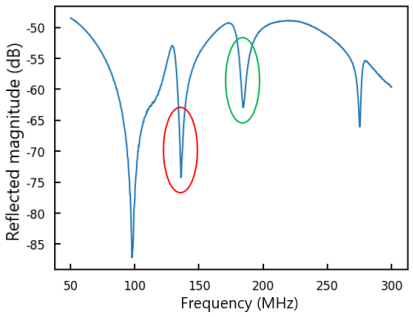

(a) Resonance dips of all four LC circuits

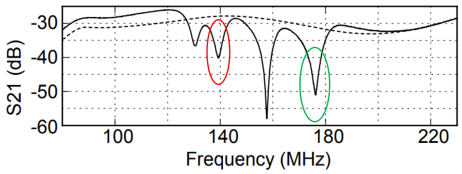

(b) Adapted from Spin interactions within a two-dimensional array of GaAs double dots [9].

Figure 26

In source [9], analogous measurements are presented. The device under investigation is the same, and a comparable experimental setup was employed, but with a different cryostat. A comparison with the resonance dips shown in figure 26b provides further insight. Two frequencies correspond to the resonance frequencies from the source [9], which are indicated in colour in figure 26a. It is also noticeable that the resonant frequencies from the reference can be found in a smaller frequency range of 120-180 MHz, compared to the frequency range of 100-300 MHz measured for this thesis. In consideration of the previous results, as well as of the restrictions imposed by the cryostats available connections and the bonding (outlined in section 4.4), the upper left quadrant is deemed appropriate for the subsequent measurements.

The objective is to monitor simultaneously the DC current to ohmic 2 and the reflected signal at the resonance frequency of the top left resonator (137.5 MHz).

The DC current sourced from ohmic 7 was grounded at ohmic 2 and floated at ohmic 22. This configuration enabled the DC current to be drained only in ohmic 2. Subsequently, gates 6 and 9 were pinched off. An RF signal of 10 mV and a DC bias of 2 mV were applied to ohmic 7. A pinch-off curve in which the reflected RF resonance frequency is shielded by increasing the voltage at gates 6 and 9 is detected at the same time. Both signal yield pinch-off behaviour when both gate 6 and gate 9 are at about -0.6 V.

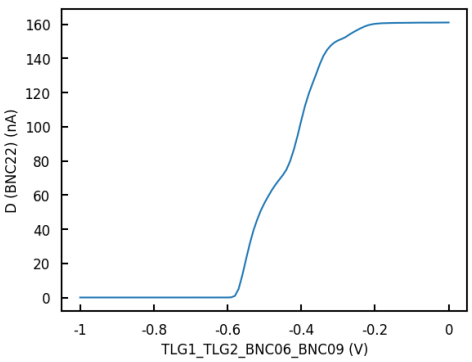

Figure 27: Pinch-off curve measured in DC.

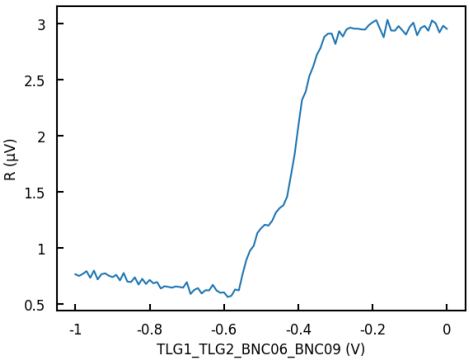

Figure 28: Pinch-off curve measured in RF.

In order to be able to draw conclusions about the research question posed

here, as to whether the RF lines in Kiutra work, the following consideration is sufficient: An RF signal is transmitted to the device via the transmission cables, and the radio frequency dip is altered by changes in the device's gate settings. Furthermore, the change is in accordance with the DC pinch-off measurements. This observation provides compelling evidence that the RF-reflectometry lines in Kiutra are functioning effectively.

5.2 SiMOS device

RF-Setup with a demodulation circuit

A stability diagram of a DQD in the few electron regime was recorded through charge sensing with direct current (DC measurement). In Figure 29b the assumed number of electrons in the two dots is given in parenthesis as (N_1, N_2), where N_1 is the number of electrons in one quantum dot and N_2 the number of electrons in the other dot.

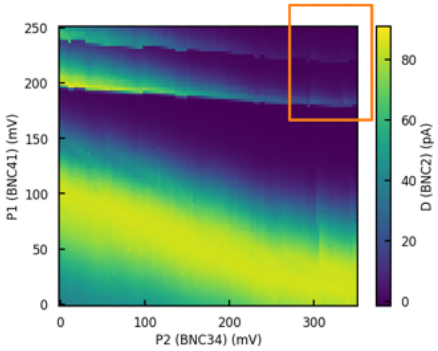

(a) Stability diagram recorded as DC measurement.

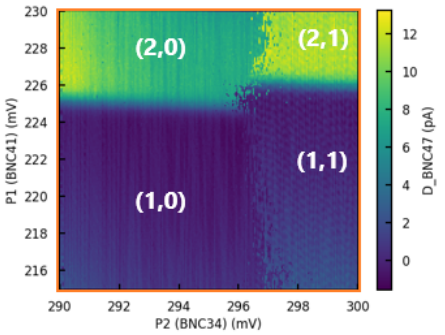

(b) Stability diagram in the few-electron regime, recorded as DC measurement. The assumed number of electrons in the two dots is given in parenthesis as (N_1, N_2).

Figure 29

The objective is to reproduce the stability diagrams previously measured in DC using RF reflectometry measurements with the setup including a demodulation circuit. In order to enhance the readout sensitivity of the setup, the frequency and phase of the RF carrier signal are to be optimized. A

frequency range of 160 MHz to 210 MHz was choosen for the subsequent finetuning of the phase. This finetuning involves the subtraction of the RF signal measured atop a Coulomb peak of the sensor dot from that measured in a Coulomb valley across various phase-frequency combinations. These measurements yield a sensitivity-enhancing map. The contrast is proportional to the slope of the Coulomb peak. Thereby, the sensitivity-enhancing map makes it possible to park at the highest possible slope on the flank of the peak, by choosing local maxima and minima on this map. Triangular markers denote two preferable parameter sets. Regions on the map that are low in difference signify areas where the RF signal remains unchanged between the Coulomb peak and valley. This indicates that the charge variations have no effect on the sensitivity of the system.

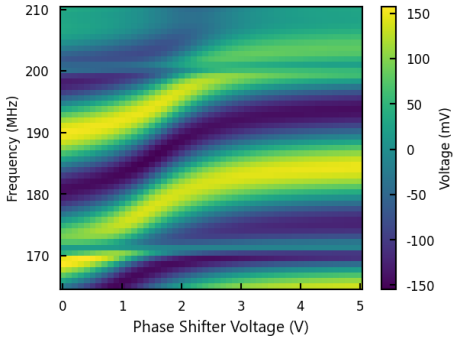

(a) Measurement of the radio frequency signal via various phase shifts. It was parked next to the Coulomb peak.

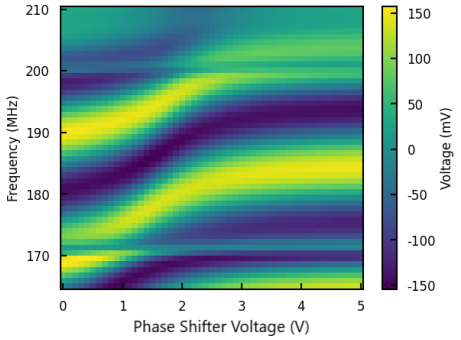

(b) Measurement of the radio frequency signal via various phase shifts. It was parked on the Coulomb peak.

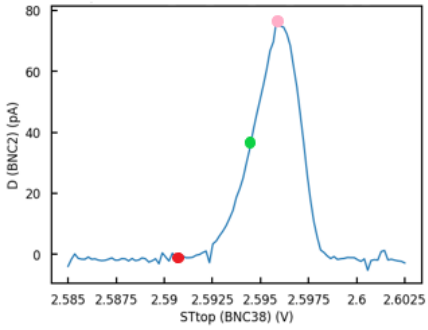

(c) Coulomb peak on which the settings for the various measurements are indicated with three different markers.

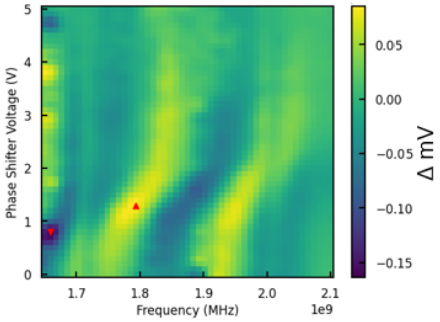

(d) Sensitivity-enhancing map, aquired by substracting on-peak and off-peak measurements.

Figure 30

No signal could be detected by the radio frequency measurements. Figures 31 and 32 illustrate a comparison between charge detection with DC and charge detection with an RF signal. It is evident that, under identical gate settings, a well-tuned double dot is recorded in DC, whereas no signal despite noise is measured in AC.

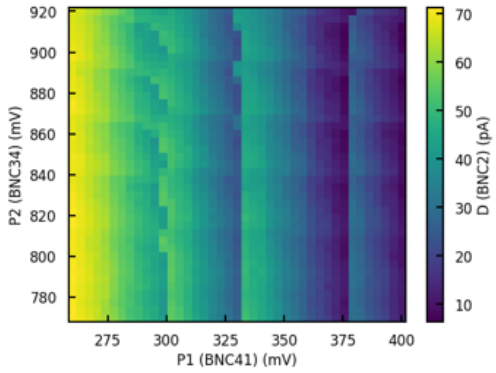

Figure 31: Stability diagram measured through charge sensing with DC current.

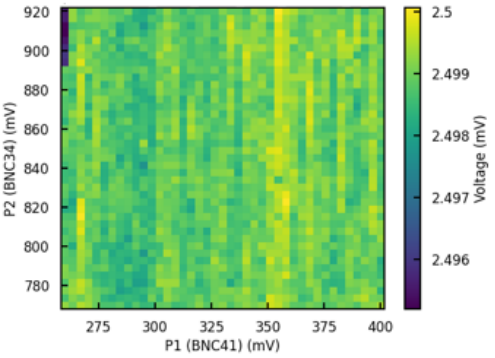

Figure 32: The attempt to measure a stability diagram by RF reflectometry.

RF-Setup with a UHF-Li

The reflectometry experiment was repeated using an UHF-Li and subsequently an additional amplifier was added in front of the signal input. Another parameter that can be optimised is the power of the RF carrier. The optimal value is the one that provides the best signal contrast, while maintaining a low temperature broadening of the Coulomb peaks. Different RF amplitudes for inputs at the UHF-Li (50 Vpk, 90 Vpk, 100 Vpk, 120 Vpk, 150 Vpk) were tested. With higher amplitudes, there is a power broadening in the coulomb peaks of the sensor dot. Despite the presence of noise, no signal could be measured for the sweeps D vs. ST, I vs. ST, Q vs. ST, R vs. ST, where ST is the plungergate of the sensor dot and the other variables are all parts of the radio frequency described in chapter 3.2. One potential explanation for the unsuccessful outcome of the RF measurements is the absence of Coulomb oscillations within the range in which there is a change in the amplitude of the radio frequency resonance. It was not possible to build a reflectometry setup with a regime suitable for RF measurements in the scope of this thesis - impedance matching failed.

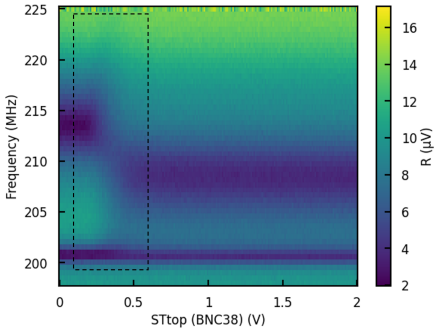

(a) Radiofrequency measured while sweeping the ST gate.

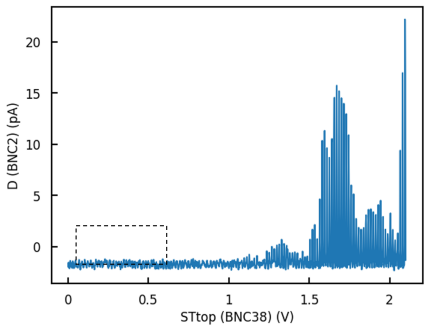

(b) Coulomb peaks measured in DC

Figure 33

Equivalent measurements were made for the test setup with the VNA, but likewise without success.

5.3 Quantum dots in Ge/SiGe

Tuning the sensor dot in RF

Regarding the structure of the following paragraph: Two samples of the same component type were measured. While only noise measurements were made for sample 1, a sensor dot was tuned and charge-sensing transitions of a nearby double dot were recorded for sample 2 in addition to the noise measurements.

Firstly, the sensor dot of sample 2 is tuned using RF reflectometry. It could only be tuned under the barrier gate B1. As can be seen in Figure 34, there are no Coulomb diamonds with defined charging energy under the plunger gate of the left sensor dot.

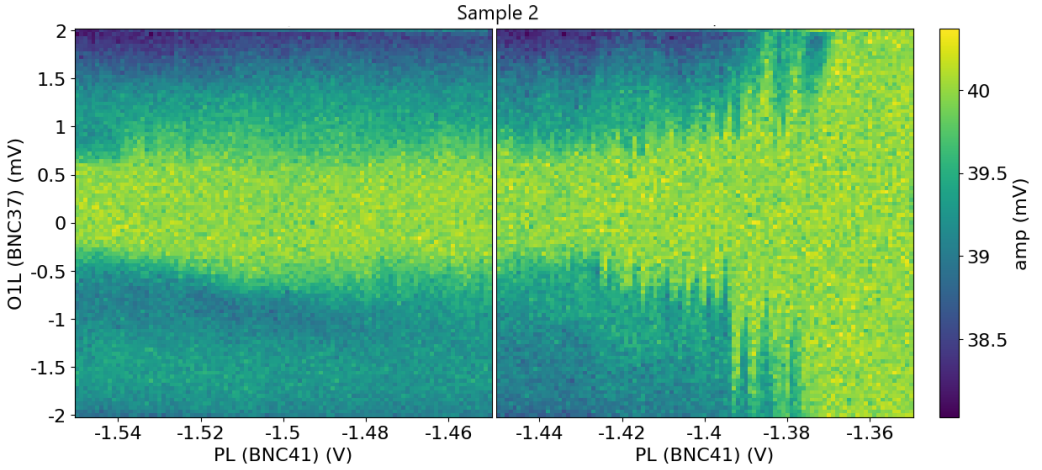

Figure 34: Bias spectroskopy with the plunger gate PL.

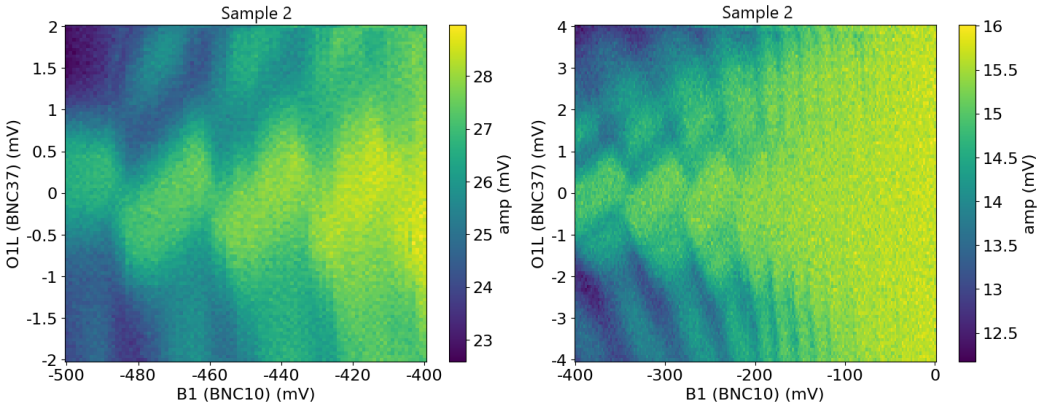

Figure 35: Bias spectroskopy with the barrier gate B1.

Figure 36: Bias spectroskopy with the barrier gate B1.

It becomes clear that the device does not have the quantum dots exactly where they should be. In order to continue making informed decisions about tuning, an attempt is made to visualise the placement of the quantum dots, piece by piece, using the results of the two-dimensional sweeps. The first version of this visualization can be seen in figure 37, where the sensor dot is assumed to be under B1.

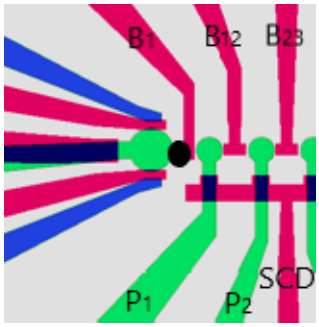

Figure 37: Schematic representation of gates and the presumed position of the sensor quantum dot, shown as a black oval.

Comparison coulomb diamonds in RF and DC

It was shown that the Coulomb diamonds are reproducible in direct transport. All gate settings were retained to ensure comparability. In the Coulomb diamonds ,both in DC and RF, not only areas with one allowed charge state transition, but also areas with two energetically allowed charge state transitions are visible.

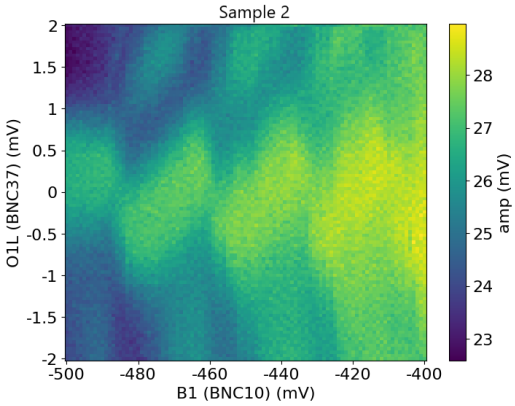

Figure 38: Coulomb diamonds measured using a RF setup.

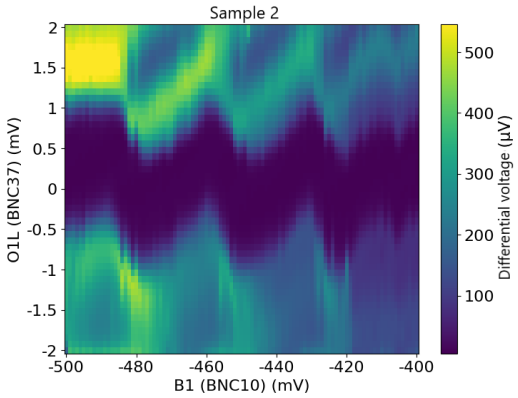

Figure 39: Coulomb diamonds measured using a DC setup.

Charge Sensing in RF

Figures 40 and 42 illustrate two-dimensional measurements obtained through voltage sweeps of different gates. In figure 40, the barrier gate B12, which

was originally intended for the coupling between the two quantum dots, and the plunger gate P2 are swept. It is important to note that B12 was only changed by 25 mV, while the plunger gate P2 was changed by 100 mV. The curvature of the charge-sensing transitions indicates that the recorded quantum dots are more strongly coupled to B12 than to P2. In figure 42, barrier gate B1 and barrier gate B12 are swept. The curvature of the charge-sensing transitions shows that the recorded quantum dots are more strongly coupled to B12 than to B1. These measurements were employed to record charge-sensing transitions, which are indicated by red lines on the adjacent copies of the measurement results (Fig. 41 and 43). The comparison with the schematic representations of the stability diagrams in chapter 2.4 suggests that these are probably two quantum dots with strong tunnelling coupling. However, the quantum dots could not be further isolated from each other by changing the gate setting and the amplitude of the radiofrequency signal. They are marked in red in the smaller images to help with visualisation.

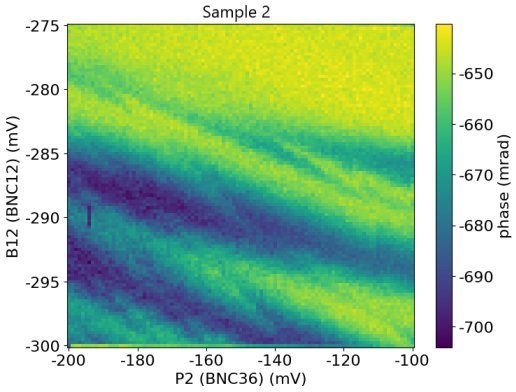

Figure 40: Charge transitions measured while sweeping a barrier gate and a plunger gate.

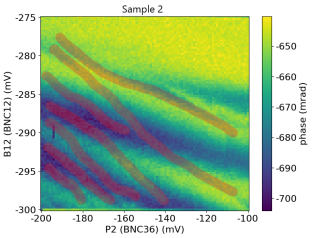

Figure 41: Copy of the adjacent plot with red lines drawn in to illustrate the charge transitions.

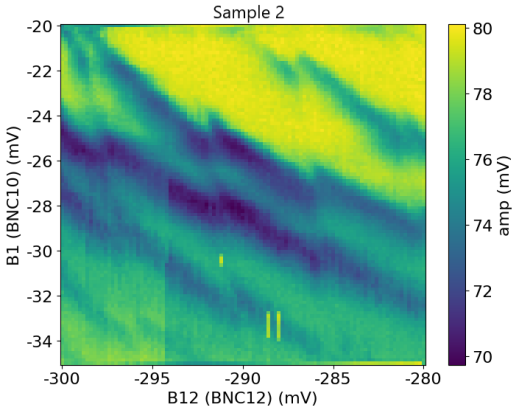

Figure 42: Charge transitions measured while sweeping two barrier gates.

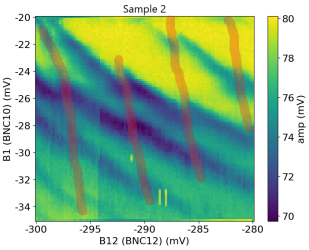

Figure 43: Copy of the adjacent plot with red lines drawn in to illustrate the charge transitions.

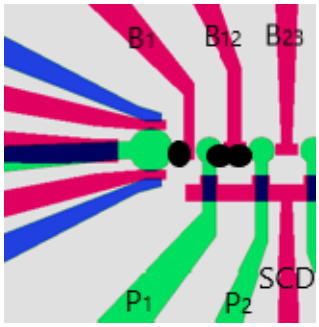

Figure 44: Schematic representation of gates and the presumed position of the sensor quantum dot as well as the DQD, shown as black ovals.

Last hole

The quantum dot located underneath P1 was tuned. Subsequently, the transitions were analysed via charge sensing using RF reflectometry, with the objective of reaching the regime in which there are only a few holes in the dot. With sufficient resolution, the final hole in the quantum dot can be identified as the final transition. Once the last hole has been identified, there are no further transitions because the quantum dot has been completely emptied of its charge carriers. The resolution, or signal-to-noise radius, is insufficient to permit the definitive conclusion that no further transitions exist. Nevertheless, the abrupt cessation of the transitions is indicative of the possibility that these may be the final charge carriers.

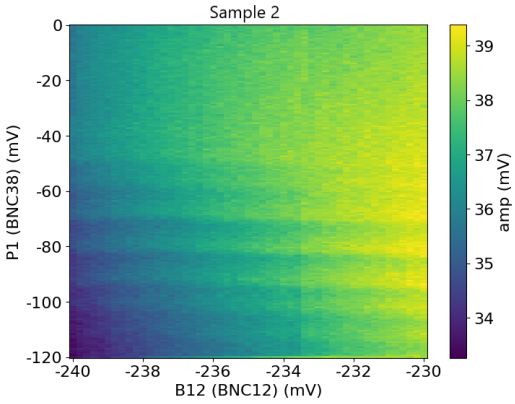

Figure 45: Charge transitions measured while sweeping a barrier gate and a plunger gate.

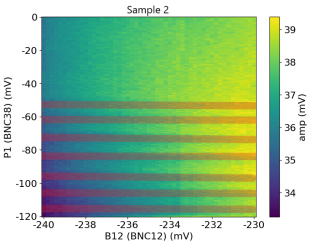

Figure 46: Copy of the adjacent plot with red lines drawn in to illustrate the charge transitions.

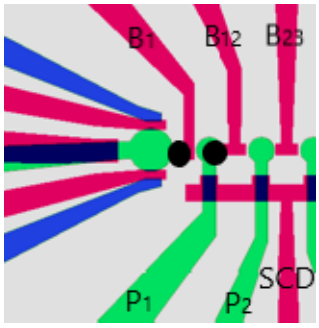

Figure 47: Schematic representation of gates and the presumed position of the sensor quantum dot as well as a single quantum dot, shown as two black ovals.

5.4 Noise testing

The bias was set to $0.4\,mV$ for both samples. Figures 48a and 48c provide schematic representations of the points on each Coulomb peak at which noise measurements are to be carried out. The points are to be located on the left and right in the blockade regime, on the flanks of the Coulomb peak and near the top of the peak. Figure 48b and 48d depict Coulomb peaks (shown in blue) and the derivatives dI/dV (shown in red), which illustrate the susceptibility of the source-drain current to fluctuations in the electric

field across all gate voltage configurations where measurements of charge noise are conducted.

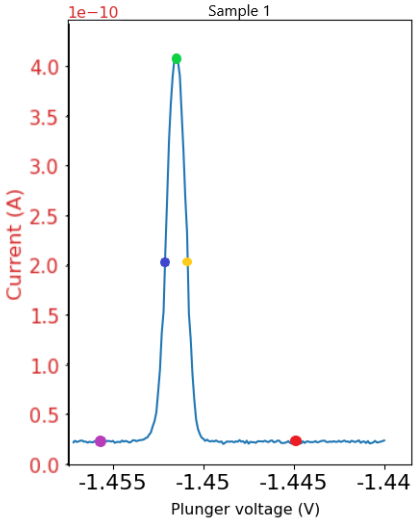

(a) Coulomb peak sensor.

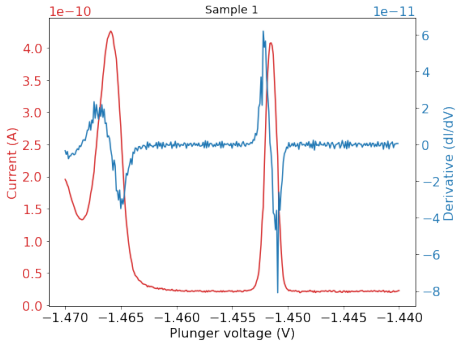

(b) Coulomb peak (blue) and its derivative (red).

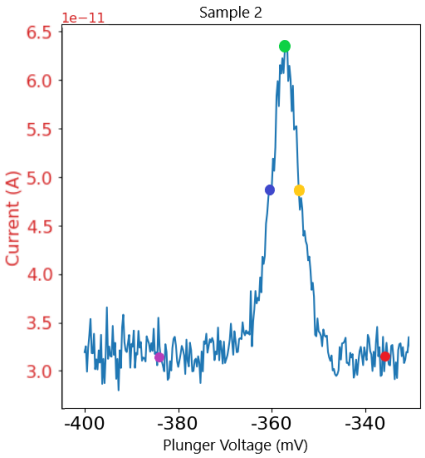

(c) Coulomb peak sensor.

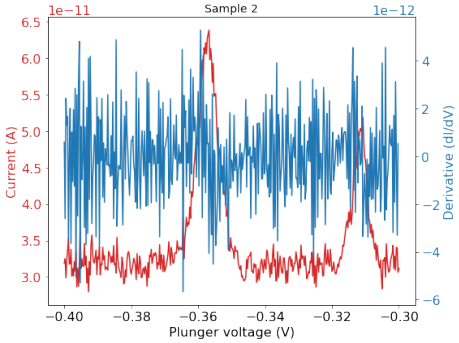

(d) Coulomb peak (blue) and its derivative (red).

Figure 48

The different time traces are coloured in accordance with the positions on the Coulomb peaks. As expected, the higher the position on the Coulomb peak, the higher the current. Subsequently, the recorded data are subjected

to processing in accordance with the methodology outlined in chapter 3.3, with the objective of obtaining the power spectral density (PSD) over frequency plots.

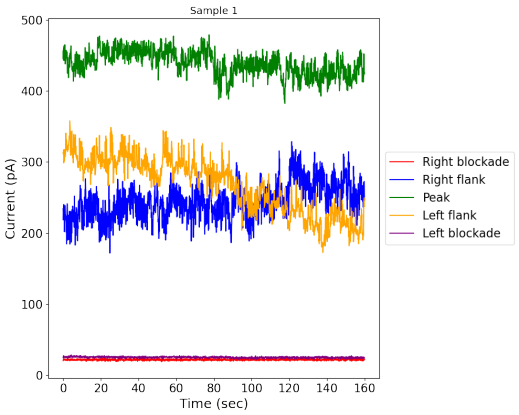

Figure 49: Time traces taken at various positions along a Coulomb peak. Sample 1

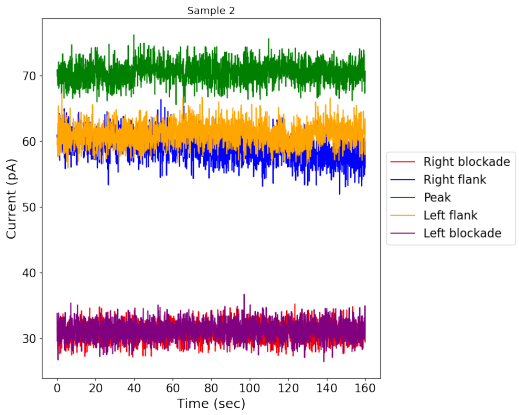

Figure 50: Time traces taken at various positions along a Coulomb peak. Sample 2

Firstly, the current noise is converted to charge noise utilising the respective dI/dV and lever arm α. The lever arms were derived from the Coulomb diamonds. For Sample 1 the lever arm is given by $\alpha_1 \approx 0.08\,\frac{eV}{V}$, and for Sample 2 it is given by $\alpha_1 \approx 0.053\,\frac{eV}{V}$. The charge noise spectra are fitted to $\frac{S_0}{f^\gamma}$. The observed spectrum exhibits a $\frac{1}{f^\gamma}$ characteristic, with the exponent γ beeing close to one for most values. Figures 51a and 51c are summaries of all PSD plots, while Figure 51b and 51d each represent one of the individual PSD plots, parked on the right flank of the Coulomb peak and with indication of the proportionality determined via the linear fit. The plots of the charge noise for the other measurements at the individual points of the Coulomb peaks can be found in the appendix.

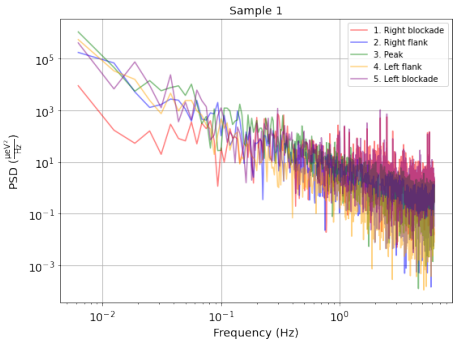

(a) Summary of all PSD plots

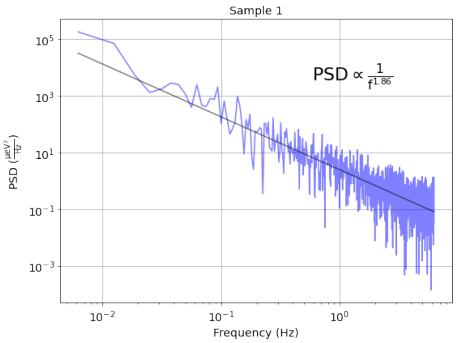

(b) One of the individual PSD plots, parked on the right flank of the Coulomb peak and with indication of the proportionality determined via the linear fit.

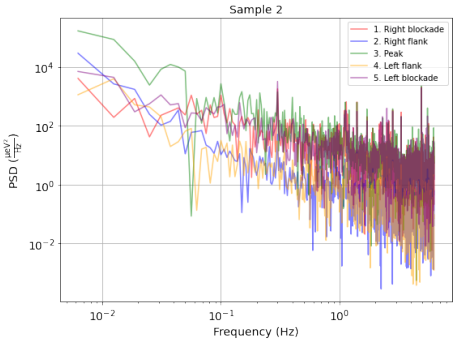

(c) Summary of all PSD plots

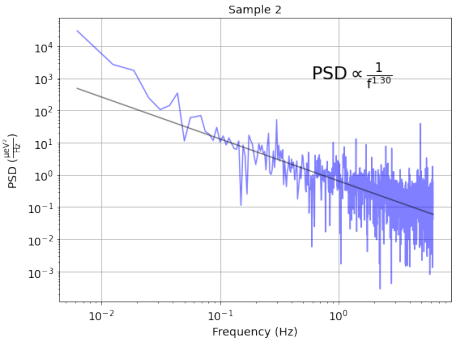

(d) One of the individual PSD plots, parked on the right flank of the Coulomb peak and with indication of the proportionality determined via the linear fit.

Figure 51

The detailed findings that are presented in Tables 4 and 5 include the exponent γ, the plunger voltage which signifies the location on the Coulomb peak as well as the $\sqrt{PSD}$ at $1\,Hz$, which serves as a figure of merit for comparing the noise level to literature. The errors indicated for the figures of merit and the exponent γ are the standard deviations of the fit generated by the Python command "perr = np.sqrt(np.diag(pcov))". Given that the figure of merit is the square root of the PSD value at 1 Hz, the error output

was converted using Gaussian error propagation. The followig formula was used:

$$f_{sqrt} = \frac{f}{2\sqrt{PSD}} \tag{11}$$

where f is the error given by the code and f_{sqrt} is the corrected error.

Placement on CP	Plunger voltage $[V]$	$\sqrt{PSD}$ at $1\,Hz$ $\left[\frac{\mu eV}{\sqrt{Hz}}\right]$	Exponent γ in arb. units
Right blockade regime	-1.4400V	2.58 ± 0.08	1.14 ± 0.06
Right flank	-1.4497V	1.57 ± 0.04	1.86 ± 0.05
Close to peak	-1.4505V	2.50 ± 0.07	1.95 ± 0.05
Left flank	-1.45078V	0.82 ± 0.02	2.24 ± 0.04
Left blockade regime	-1.4520V	3.02 ± 0.09	1.53 ± 0.05

Table 4: The detailed findings for sample 1.

Placement on CP	Plunger voltage $[V]$	$\sqrt{PSD}$ at $1\,Hz$ $\left[\frac{\mu eV}{\sqrt{Hz}}\right]$	Exponent γ in arb. units
Right blockade regime	-0.340V	3.59 ± 0.11	0.98 ± 0.05
Right flank	-0.356V	0.81 ± 0.02	1.30 ± 0.05
Close to peak	-0.358V	4.61 ± 0.15	1.26 ± 0.05
Left flank	-0.360V	0.82 ± 0.02	1.25 ± 0.05
Left blockade regime	-0.380V	3.64 ± 0.11	1.02 ± 0.05

Table 5: The detailed findings for sample 2.

Comparison to literature

The noise characteristics of planar Ge/SiGe heterostructures were also investigated within the context of the paper "Low percolation density and charge noise with holes in germanium" by Mario Lodari et.al. [18]. The researchers concluded that Ge heterostructures support the quiet operation of hole quantum dots. Figure 52, depicts the measured power spectral density S_E, which is the same physical quantity as the PSD, is parked at $V_P = -698.8\,mV$ on one of the flanks of the Coulomb peak. The lever arm is $\alpha \approx 0.1\,\frac{eV}{V}$. This plot is similar in form to the ones measured in the scope of this thesis and

especially sample 2 has similar values for the exponent. However, it should be noted that the measured frequency range is slightly different. The spectral pattern exhibits a 1/f trend at lower frequencies, enabling the derivation of a charge noise value at 1 Hz. Out of 6 different devices, always parked on the flanks of the Coulomb peak, the average charge noise level at $1\,Hz$ was $\overline{\sqrt{S_E}} = 0.62\,\frac{\mu eV}{\sqrt{Hz}}$. A comparison of this averaged value and the $\sqrt{PSD}$ at $1\,Hz$ determined as part of this thesis are plotted in Figure 53.

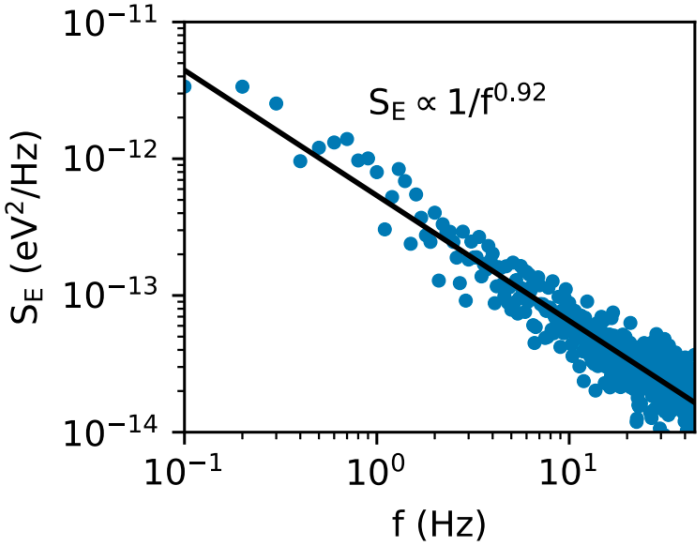

Figure 52: The power spectrum density of the noise picked up by a quantum dot is presented for a plunger gate voltage of $V_P = -698.8\,mV$. The solid line represents a linear fit to the data, which yielded a slope of -0.92. Taken from source [18].

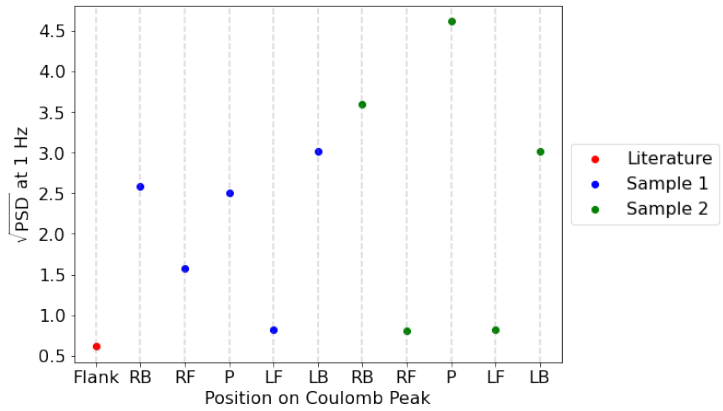

Figure 53: The literature value $\overline{\sqrt{S_E}} = 0.62 \frac{\mu eV}{\sqrt{Hz}}$ is an averaged result taken from source 18. The abbreviations shown on the x-axis signify the locations on the Coulomb peak. RB = Right blockade, RF = Right flank, P = Peak, LF = Left flank, LB = Left blockade.

In conclusion, it can be stated that the values measured on the flanks of the Coulomb peaks, in particular, are in close agreement with the values reported in the literature. This suggests that low-noise operations may be feasible with this type of device.

6 Conclusion and outlook

The first experiment in this thesis was carried out on a GaAs component with the aim of testing the transmission lines of the Kiutra cryostat. The resonance frequencies of all four tank circuits were successfully measured. This indicated that a signal was being received by the device and was being correctly returned to the measuring instruments. Subsequently, a resonance frequency was selected and a pinch-off curve was measured. The resulting pinch-off curve could be reproduced with a DC measurement, and a similar pinch-off behaviour was found. This outcome can be regarded as a further indication that the RF lines in Kiutra are functioning as intended. The second experiment involved the investigation of a SiMOS component. The objective was to initially conduct charge sensing and the requisite tuning of the quantum dots through DC measurements. Subsequently, the aim was to reproduce these results through RF reflectometry measurements. The tuning and charge sensing measurements in DC were successfully carried out, and clear charge transitions were visible in the stability diagrams. However, despite the implementation of three different reflectometry setups and optimization attempts, no signal apart from noise could be measured. Experiments from two different categories were carried out on the third device, which is a Ge/SiGe device. On the one hand, a sensor dot and a double quantum dot were tuned using RF reflectometry. The difficulty with this experiment was, that the quantum dots were not where they were supposed to be in the gate structure. The sensor dot was situated underneath the barrier gate that should have been used to confine the DQD and control the capacitive coupling between the sensor dot and the DQD. Charge transitions of the DQD could be detected, however, they were strongly coupled and it was not possible to seperate them into two seperate dots. Bias spectroscopy measurements could be carried out in both radiofrequency (RF) and direct current (DC), allowing for the juxtaposition of Coulomb diamonds in DC and RF under equivalent gate settings. On the other hand, noise measurements were carried out on two samples of the Ge/SiGe component. The power spectral density was calculated and reference values at 1Hz were extracted and compared with literature values. The values measured on the flanks of the Coulomb peaks, in particular, are in close agreement with the values reported in the literature. Now it is important to think about possible future steps after these partially successful and partially unsuccessful experiments. The experiment with the GaAs device was successfully completed. It should

be noted that some of the electrical connections of the gates did not correspond to the available connections in the Kitura cryostat. Consequently, several gates could not be used. One possible question to be addressed is whether there is a universal bonding scheme that is suitable for the electrical connections in the different cryostats. For the SiMOS component, it will be important to continue the problem analysis by systematically replacing the individual components of for example the demodulation circuit one after the other. For the Ge/SiGe component, the energies between the individual transitions in one quantum dot could be calculated and compared to the filling of orbitals in atoms. Furthermore, a subsequent step could be the inclusion of magnetic fields to perform magneto spectroscopy.

References

1. *Spin Qubits in Silicon and Germanium*
   Lawrie, W. I. L. (2022). Dissertation (TU Delft), Delft University of Technology

2. *Fast Charge Sensing of Si/SiGe Quantum Dots via a High-Frequency Accumulation Gate*
   Rainwater, Greg, Christian Volk, et al. Nano Letters 2019, 19 (8), 5628-5633. DOI: 10.1021/acs.nanolett.9b02149

3. *Semiconductor Spin Qubits*
   Guido Burkard et al. Rev. Mod. Phys. 95, 025003 – Published 14 June 2023

4. *Bluefors*
   URL: https://bluefors.com/products/dilution-refrigerator-measurement-systems/

5. *Kiutra*
   URL: https://kiutra.com/products/l-type-rapid/

6. *Electron transport through double quantum dots*
   W. G. van der Wiel et al. Reviews of Modern Physics, Volume 75, January 2003

7. *Probing quantum devices with radio-frequency reflectometry*
   Florian Vigneau et al. 23 February 2022

8. *Molecular beam epitaxy of germanium quantum wells with low surface roughness*
   Charalampos Lampadaris, et al. February 9, 2024

9. *Spin interactions within a two-dimensional array of GaAs double dots*
   Federico Fedele

10. *Chip design and details*
    Harry Lampdadaris, 4 April 2024

11. *Automation of tuning strategies for spin qubits from 2DEG to quantum dot*
    Lara Lausen

12. *The Physical Implementation of Quantum Computation*
David P. DiVincenzo, Fortschr. Physik 48 (2000)

13. *Quantum Computation and Quantum Information*
Nielsen, Michael A., and Isaac L. Chuang. Cambridge University Press, 2010

14. *Few Electron Double Quantum Dots for a Circuit QED Architecture*
Anna Stockklauser, Zurich, July 12, 2012

15. *A flexible 300 mm integrated Si MOS platform for electron- and hole-spin qubits exploration*
R. Li et al.

16. *Semiconductor nanostructures: quantum states and electronic transport*
T. Ihn, Oxford University Press, 2015

17. *Non-equilibrium thermodynamics in a single-molecule quantum system*
Pyurbeeva, Eugenia et.al.,2023,Materials for Quantum Technology, doi = 10.1088/2633-4356/accd3a

18. *Low percolation density and charge noise with holes in germanium*
Mario Lodari et al 2021 Mater. Quantum. Technol. 1 011002

19. *Low charge noise quantum dots with industrial CMOS manufacturing*
A. Elsayed

20. *Coulomb blockade in quantum dots*
A. Fuhrer and C. Fasth, April 2007

21. *Signal Theory. Information theory.*
Franks, L.E. (September 1969). Englewood Cliffs, NJ: Prentice Hall. ISBN 0138100772

22. *Kiutra*
URL::https://kiutra.com/products/l-type-rapid/

23. *Bluefors*
URL:https://bluefors.com/products/dilution-refrigerator-measurement-systems/

7 Appendix

7.1 Kiutra

Figure 54: A photo of the Kiutra cryostat taken from the manufacturer's website. [22]

A list of key data:

- Temperature range: $100mK$–$300K$
- Sample cooldown time $< 3h$
- Continuous operation above $300mK$
- 4T z-axis magnet
- Cooling mechanism: (continuous) adiabatic demagnetization refrigeration
- Cryogenic-free (no 3He)
- 1xRF reflectometry line
- 2xRF fast lines

Kiutra's interior and the demodulation circuit

A comprehensive overview of Kiutra's interior with the demodulation circuit suited for rf reflectometry beeing implemented:

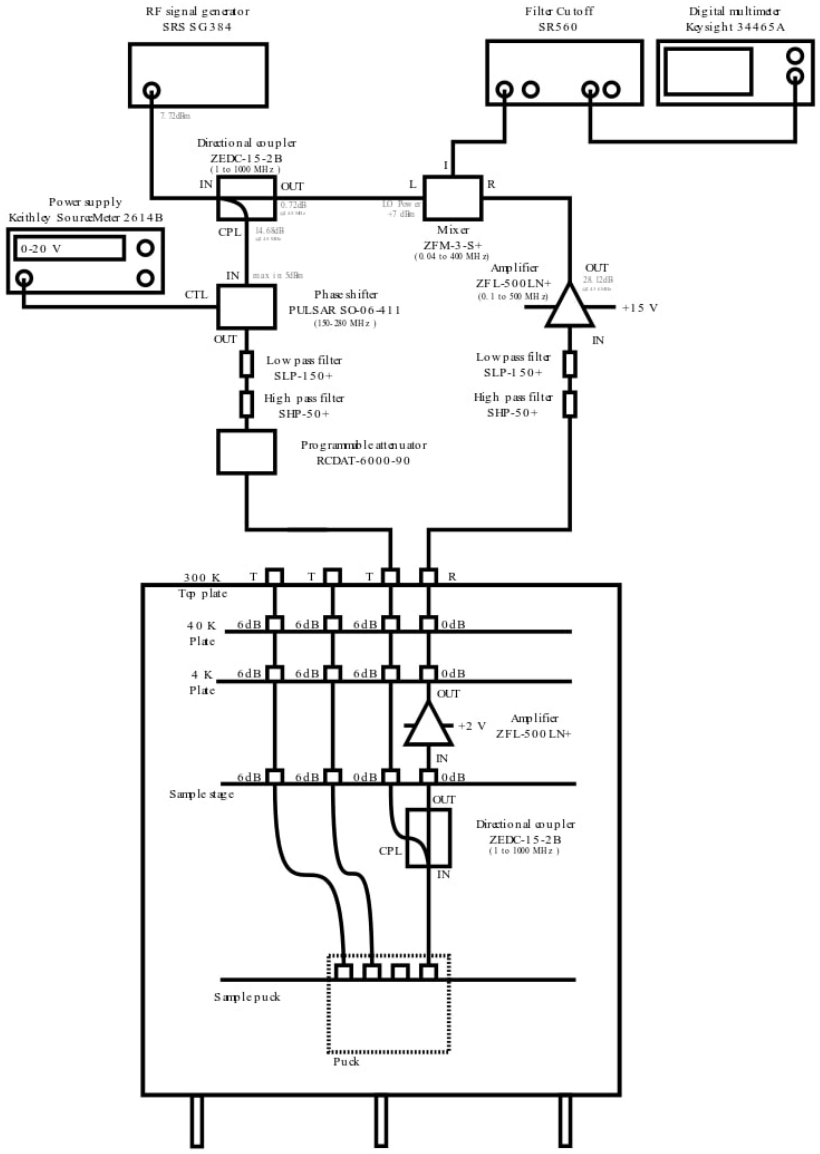

7.2 Bluefors

Figure 55: A photo of the Bluefors cryostat taken from the manufacturer's website. [23]

A list of key data:

- Temperature down to 20mK (continuous)
- Sample cooldown time 12h to 20h (with bottom loader)
- 6/1/1 T magnet
- Cooling mechanism: dilution refrigeration
- Up to 2xRF reflectometry lines
- Up to 20xRF fast lines

7.3 Noise measurements - Extended presentation of plots

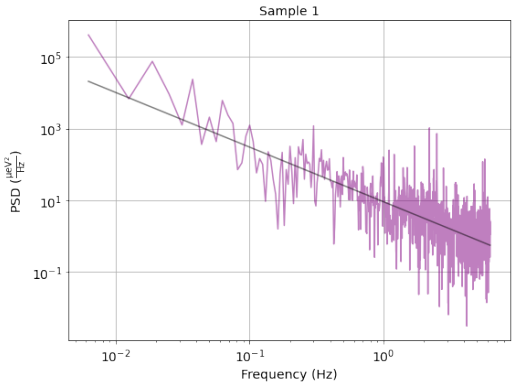

Figure 56: Left blockade regime

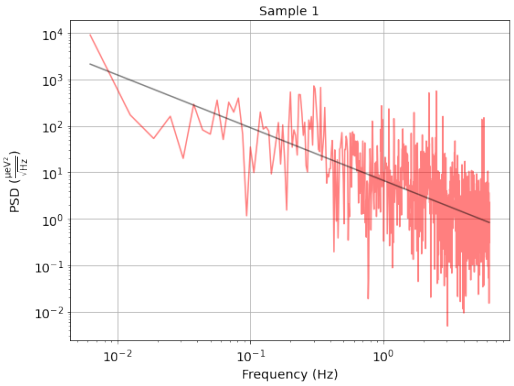

Figure 57: Right blockade regime

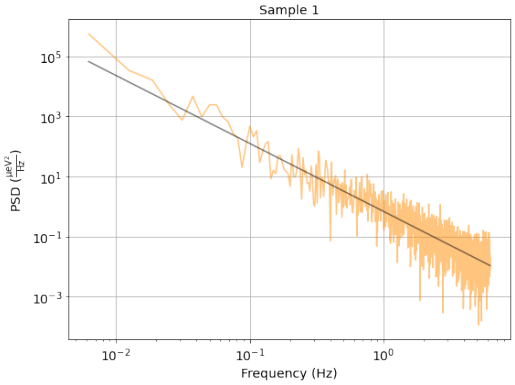

Figure 58: Left flank

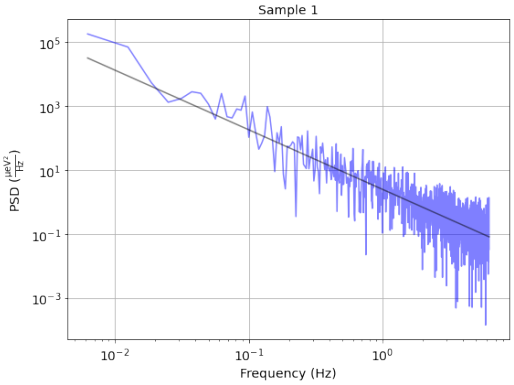

Figure 59: Right flank

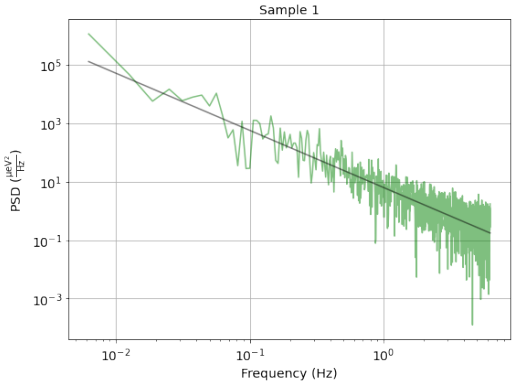

Figure 60: Close to the peak

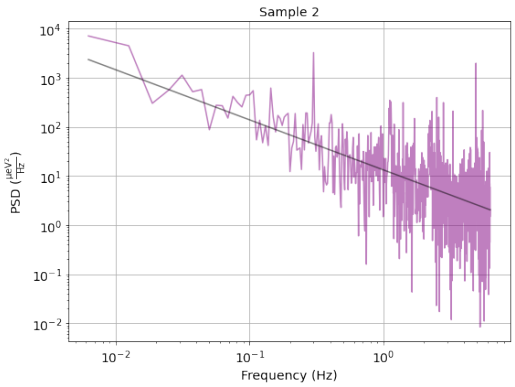

Figure 61: Left blockade regime

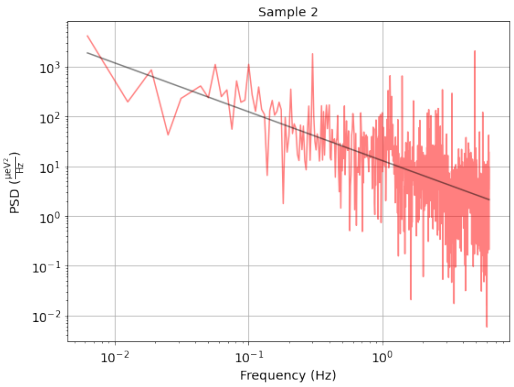

Figure 62: Right blockade regime

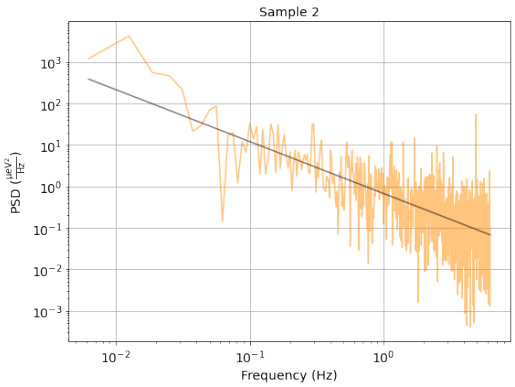

Figure 63: Left flank

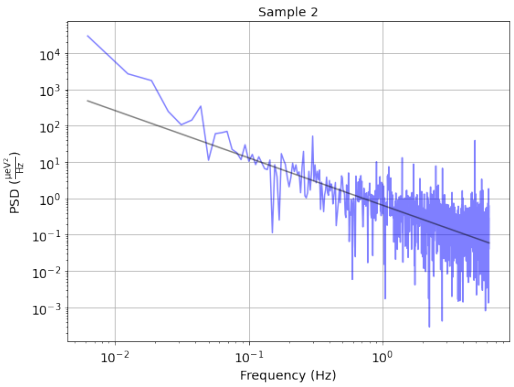

Figure 64: Right flank

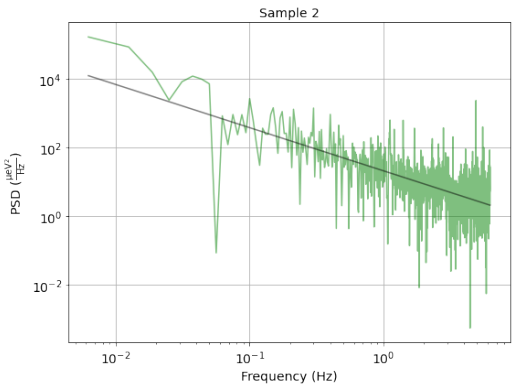

Figure 65: Close to the peak